The genesis of the ores and granitic rocks at the Hongshi Au deposit in Eastern Tianshan, China: Constraints from zircon U–Pb geochronology, geochemistry and isotope systematics

Yin-Hong Wang [a,*], Chun-Ji Xue [a], Jun-Bao Gao [b], Fang-Fang Zhang [a], Jia-Jun Liu [a], Jian-Ping Wang [a], Ji-Chun Wang [a]

[a] State Key Laboratory of Geological Processes and Mineral Resources, China University of Geosciences, Beijing 100083, China
[b] No. 1 Geological Party, Xinjiang Bureau of Geology and Mineral Exploration, Changji 831100, China

ABSTRACT

The Hongshi gold deposit is located in the southwestern margin of the Kanggur–Huangshan ductile shear zone in Eastern Tianshan, Northwest China. The gold ore bodies are predominantly hosted in the volcanogenic metasedimentary rocks of the Lower Carboniferous Gandun Formation and the Carboniferous syenogranite and alkali-feldspar granite. The syenogranite and the alkali-feldspar granite yield SHRIMP zircon U–Pb ages of 337.6 ± 4.5 Ma (2σ, MSWD = 1.3) and 334.0 ± 3.7 Ma (2σ, MSWD = 1.1), respectively, indicating that the Hongshi gold deposit is younger than 334 Ma. The granitoids belong to shoshonitic series and are relatively enriched in large ion lithophile elements (Rb, K, Ba, and Pb) and depleted in high field-strength elements (Nb, Ta, P, and Ti). Moreover, these granitoids have high SiO_2, Al_2O_3, and K_2O contents, low Na_2O, MgO, and TiO_2 contents, low Nb/Ta ratios, and slightly positive Eu anomalies. The $\varepsilon_{Hf}(t)$ values of the zircons from a syenogranite sample vary from $+1.5$ to $+8.8$ with an average of $+5.6$; the $\varepsilon_{Hf}(t)$ values of the zircons from an alkali-feldspar granite sample vary from $+5.0$ and $+10.1$ with an average of $+7.9$. The $\delta^{34}S$ values of 10 sulfide samples ranged from $-11.5‰$ to $+4.2‰$, with peaks in the range of $+1‰$ to $+4‰$. The above-mentioned data suggest that the Hongshi granitoids were derived from the melting of juvenile lower crust mixed with mantle components formed by the southward subduction of the paleo-Tianshan ocean plate beneath the Aqishan–Yamansu island arc during the Early Carboniferous. The Hongshi gold deposit was formed by post-collisional tectonism during the Permian. The granitoids most likely acted as impermeable barriers that prevented the leakage and runoff of ore-bearing fluids. Thus, the granitoids probably played an important role in controlling gold mineralization.

1. Introduction

The Central Asia Orogenic Belt (CAOB) is a well-known Phanerozoic orogenic collage that is composed of microcontinental blocks, island arcs, oceanic crustal remnants, and continental marginal facies rocks (e.g., Goldfarb et al., 2014; Kovalenko et al., 2004; Mao et al., 2014; Pirajno, 2010; Xiao et al., 2010). The formation of the CAOB was caused by multiple accretion and arc–continent collision events that occurred from the Early Neoproterozoic to the Permian and were driven by the successive closure of the paleo-Asian Ocean (Li et al., 2013; Sengor et al., 1993; Shen et al., 2013; Windley et al., 2007; Xiao et al., 2010). The Eastern Tianshan belt is one of China's important gold metallogenic belts (Fig. 1A; Huang et al., 2013; Wang et al., 2015a, 2015b, 2015c) and

hosts over 30 gold deposits and occurrences (Charvet et al., 2007; Chen et al., 2014; Pirajno et al., 1997; Pirajno, 2013; Qin et al., 2002; and references therein). In the Eastern Tianshan belt, the orogenic gold deposits (e.g., Hongshi, Kanggur, Matoutan, Jinwozi, and Hongshan) are economically important and are primarily emplaced along the Kanggur–Huangshan ductile shear zone (Fig. 1C; Table 1; Y.J. Chen et al., 2007; Rui et al., 2002; Wang et al., 2015c; Zhang et al., 2014). These orogenic gold deposits are thought to be hosted in intermediate-felsic volcanic and pyroclastic rocks and are spatially associated with local intrusions (Y.J. Chen et al., 2005, 2007; Wang et al., 2015c; Zhang et al., 2014), but the geneses, ages and geodynamic settings of intrusive rocks and their genetic relationships with gold mineralization remain unclear (Y.J. Chen et al., 2012; Rui et al., 2002; Wang et al., 2015c; Zhang et al., 2003a).

The Hongshi gold deposit, which was discovered in 1996 during a regional mapping and geochemical survey (Cao et al., 2010), is one of the orogenic gold deposits in Eastern Tianshan. The zircon LA–ICP–MS U–Pb age of a granitic intrusion located in the southern Hongshi area was
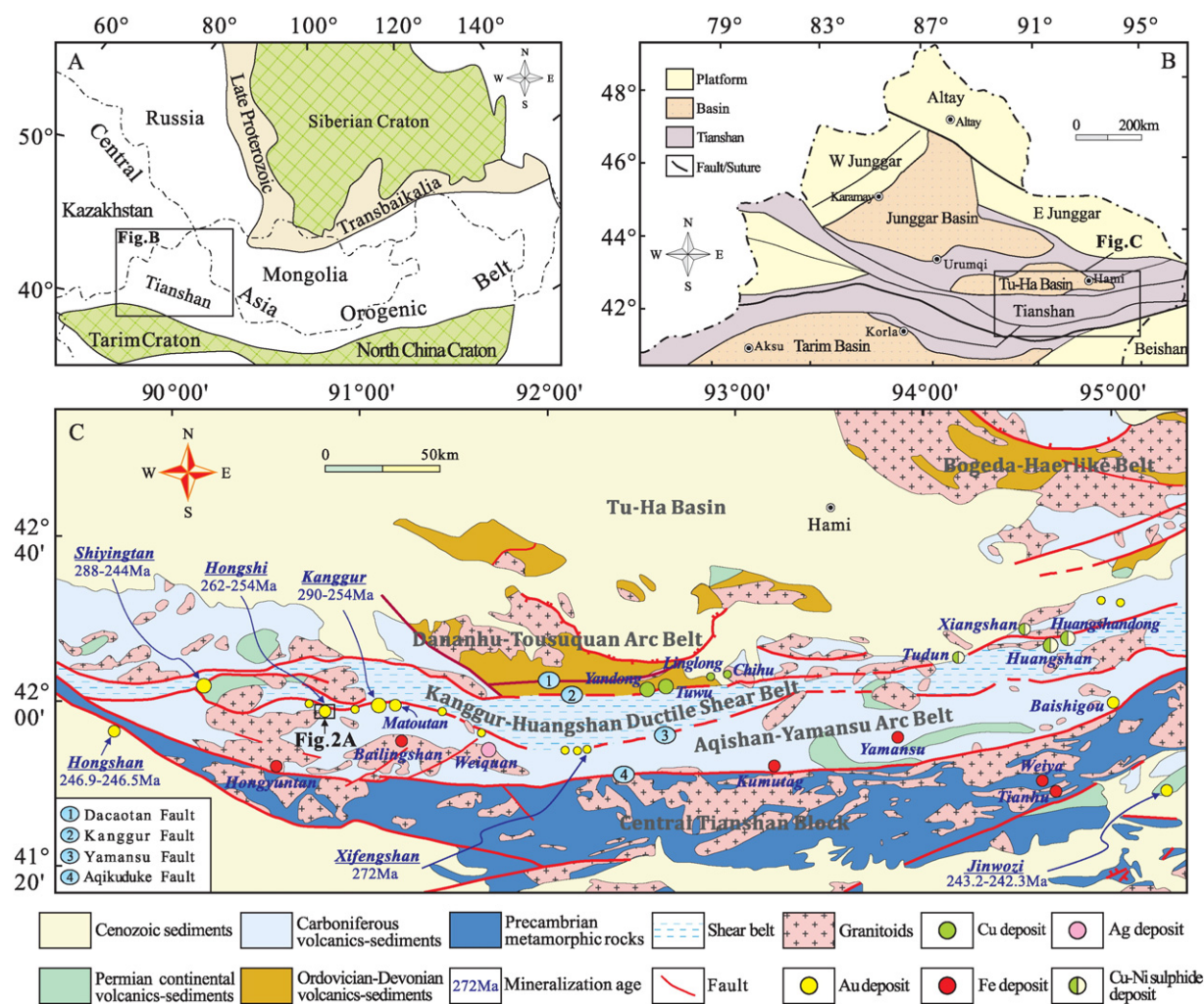
Fig. 1. (A) Location of the study area in the Central Asia Orogenic Belt (modified from Huang et al. (2013)). (B) Sketch map showing the geological units of the Tianshan Belt (modified from Y.J. Chen et al. (2012)). (C) Simplified geological map of the Eastern Tianshan Belt (modified from J.B. Wang et al. (2006)).

reported by Zhou et al. (2010) to be 282.7 ± 4.2 Ma. Sun et al. (2012) reported a zircon SHRIMP U–Pb age of 344 ± 4 Ma for the syenogranite and also estimated 262 ± 1 Ma as the time of mineralization in the Hongshi deposit based on the ^{39}Ar–^{40}Ar plateau age of altered sericite. Until now, the gold mineralization features and ore-forming mechanism have not been adequately constrained, largely because of a lack of detailed geochemical and geochronological data for this deposit. In this study, we present whole-rock geochemistry data, SHRIMP zircon U–Pb dating, and in situ Lu–Hf isotopes of the Hongshi granitoid intrusions. We also present sulfide isotopic data for the Hongshi deposit. We further discuss the temporal and genetic relationship between the formation of the Hongshi deposit and the tectonic evolution of Eastern Tianshan during the Late Paleozoic.

2. Geological setting

2.1. Regional geology

The Eastern Tianshan orogenic belt is ca. 300 km wide bounded by the Junggar Basin to the north and the Tarim Basin to the south (Fig. 1B; Y.J. Chen et al., 2012). This belt is one of the important producers of Cu (+/−Ni), Au, Fe, and Ag in the CAOB (e.g., Y.J. Chen et al., 2007; Deng et al., 2014; Deng and Wang, 2015; Mao et al., 2005; Pirajno, 2010, 2013; Zhai et al., 1999, 2011). The Eastern Tianshan belt experienced a long and complex tectonic evolution that included continental breakup, oceanic crust subduction, continental growth,

continental collision, and intracontinental tectonic deformation (Charvet et al., 2007; Pirajno, 2013; Xiao et al., 2013; Wang et al., 2015c, 2015d). The Eastern Tianshan belt is divided into three major tectonic zones—the Dananhu–Tousuquan arc belt, the Kanggur–Huangshan ductile shear zone, and the Aqishan–Yamansu arc belt. These three zones are separated by the Kanggur and Yamansu faults (Fig. 1C).

Situated in the northern Kanggur Fault, the northern Dananhu–Tousuquan arc belt is primarily composed of Ordovician–Silurian calc-alkaline volcanic rocks along with Devonian–Carboniferous mafic and pyroclastic rocks, calc-alkaline felsic volcanic rocks, greywacke, and carbonates (Qin et al., 2011; Xue et al., 1995; Zhang et al., 2003a). The Dananhu Unit was intruded by tonalite, granodiorite, diorite porphyry, and granodiorite porphyry with adakitic affinity. This unit is temporally and genetically associated with several porphyry Cu deposits, including the Tuwu, Yandong, Linglong, and Chihu deposits. These granitic intrusions and porphyry deposits were possibly formed during an accretionary event during the Late Carboniferous (Xiao et al., 2013; Wang et al., 2015a, 2015b).

Located between the Yamansu and Aqikuduke Faults, the southern Aqishan–Yamansu arc belt primarily comprises volcanic rocks that are Devonian–Carboniferous to Permian in age along with pyroclastic and sedimentary rocks (Xiao et al., 2010, 2013). Devonian basalt, andesite, and turbidite are intercalated with weakly metamorphosed, fine-grained clastic sediments, and carbonates and are overlain by Carboniferous andesite, basalt, dacite, rhyolite, spilite, and keratophyre. Certain

Table 1
Isotopic ages of the major gold deposits and host rocks in Eastern Tianshan.

Deposits	Dating samples		Dating methods	Ages (Ma)	References
Hongshan Au	Ores	Sericite	^{39}Ar–^{40}Ar plateau	246.9 ± 1.4	Chen et al. (2006)
		Sericite	^{39}Ar–^{40}Ar plateau	246.5 ± 1.1	Chen et al. (2006)
Shiyingtan Au	Ores	Fluid inclusion of auriferous quartz vein I	Rb–Sr isochron	288 ± 7	Zhang et al. (2003b)
		Fluid inclusion of auriferous quartz vein II	Rb–Sr isochron	246 ± 7	Zhang et al. (2003b)
		Fluid inclusion of auriferous quartz vein III	Rb–Sr isochron	244 ± 9	Zhang et al. (2003b)
	Host rocks	K-feldspar granite	LA-ICP-MS zircon U–Pb	342 ± 11	Zhou et al. (2010)
		Andesite	Rb–Sr isochron	285 ± 12	Zhang et al. (2003b)
		Granite porphyry	Rb–Sr isochron	266 ± 3	Zhang et al. (2003b)
		Tonalite	Rb–Sr isochron	293 ± 1	Li et al. (1998)
		Granodiorite	Zircon U–Pb	287 ± 3	Li et al. (1998)
Hongshi Au	Ores	Sericite	^{39}Ar–^{40}Ar plateau	253.9 ± 1.8	W. Chen et al. (2007)
		Sericite	^{39}Ar–^{40}Ar plateau	258.7 ± 1.3	W. Chen et al. (2007)
		Fluid inclusion of auriferous quartz vein	Rb–Sr isochron	257 ± 4	Sun et al. (2013)
		Sericite in altered rock	^{39}Ar–^{40}Ar plateau	262 ± 1	Sun et al. (2012)
	Host rocks	Alkali-feldspar granite	SHRIMP zircon U–Pb	344.0 ± 3.7	This study
		Syenogranite	SHRIMP zircon U–Pb	337.6 ± 4.5	This study
Kanggur Au	Ores	Altered andesite, stage I	Rb–Sr isochron	290 ± 5	Zhang et al. (2002)
		Magnetite and pyrite, stage II	Sm–Nd isochron	290.4 ± 7	Zhang et al. (2002)
		Fluid inclusion of auriferous quartz vein, stage II	Rb–Sr isochron	282.3 ± 5	Zhang et al. (2002)
		Fluid inclusion of auriferous quartz vein, stage IV	Rb–Sr isochron	258 ± 21	Zhang et al. 2002
		Fluid inclusion of auriferous quartz vein, stage V	Rb–Sr isochron	254 ± 7	Zhang et al. 2002
	Host rocks	Rhyolite porphyry	Rb–Sr isochron	300 ± 13	Zhang et al. (2002)
		Quartz–syenite porphyry	Rb–Sr isochron	282 ± 16	Zhang et al. (2002)
		Tonalite	Zircon U–Pb	275 ± 7	Zhang et al. (2002)
Xifengshan Au	Ores	Fluid inclusion of auriferous quartz vein	Rb–Sr isochron	272 ± 3	Zhang et al. (1999)
	Host rocks	Granodiorite	LA-ICP-MS zircon U–Pb	349 ± 3.4	Zhou et al. (2010)
Jinwozi Au	Ores	Sericite	^{39}Ar–^{40}Ar plateau	243.2 ± 1.8	Wang et al. (2008)
		Sericite	^{39}Ar–^{40}Ar isochron	242.3 ± 3.7	Wang et al. (2008)
	Host rocks	Granodiorite	Rb–Sr isochron	354 ± 31	Chen et al. (1999)

Upper Carboniferous andesite and rhyolite are interbedded with clastic sediments and limestones. The Lower Carboniferous lithologies can be subdivided upwards into three formations: (1) the Nanbeidagou Formation, which is composed of limestone and mylonitic carbonate; (2) the Aqishan Formation, composed of basalt, andesite, tuff, and volcanic breccia with intercalated sandstone; (3) the Yamansu Formation, composed of clastics, spilite, and keratophyre (Xiao et al., 2013). The arc belt contains sparsely distributed Permian volcanic–sedimentary rocks that are mainly composed of sandstone, siltstone, basalt, andesite, and rhyolite (Mao et al., 2005; Yang et al., 1996). The Aqishan–Yamansu arc belt also contains some Fe (− Cu) and Cu–Ag–Pb–Zn skarn deposits; for example, the Yamansu, Hongyuntan, Bailingshan, and Weiquan Formations were formed during the emplacement of granitic intrusions with associated hydrothermal activity (Mao et al., 2005).

Lying between the Kanggur and Yamansu Faults, the central Kanggur–Huangshan ductile shear zone mainly contains basalt lavas and pyroclastic rocks that were thrust southward over the Aqishan–Yamansu arc (Xiao et al., 2010, 2013). These volcanic rocks are subdivided into two major tectonic assemblages: (1) the coherent strata in the south, which include several early to mid-Carboniferous volcano-sedimentary rocks; (2) the mélanges and broken formations in the north, which include several Devonian–Carboniferous volcano-sedimentary rocks that were partly mylonitized, imbricated, and structurally repeated by thrusts (Xiao et al., 2013; Yang et al., 1996). The ductile shear zone is over 500 km in length and 10–30 km wide; it trends EW, dips N, and is characterized by a series of mylonite and mylonitized rocks. A typical metamorphic mineral assemblage primarily contains actinolite, biotite, and chlorite, which suggests that the metamorphic grade is the lower greenschist facies. The ductile shear zone is intruded by numerous Late Paleozoic mafic–ultramafic complexes, quartz porphyry, monzogranite, syenogranite, and granite porphyry; some of the intrusions have Late Carboniferous to Early Permian isotopic ages (Han et al., 2006; Mao et al., 2005; Wang et al., 2014, 2015c). The Kanggur–Huangshan ductile shear zone also contains a series of epithermal Au, orogenic-type Au and magmatic Cu–Ni sulfide mineral deposits with ages of ca. 290–250 Ma (Mao et al., 2005; Pirajno et al., 2011; Yang et al., 2009). These deposits are considered to be associated with Permian post-collision tectonism (Mao et al., 2005; Pirajno et al., 2011).

2.2. Deposit geology

The Hongshi gold deposit is situated in the northern margin of the Aqishan–Yamansu arc belt, approximately 30 km west of the Kanggur gold deposit; its geographic coordinates are 90°50′15″–90°51′40″E, 42°03′35″–42°04′18″N (Fig. 1C; J.B. Wang et al., 2006). The Hongshi gold deposit is controlled by syntectonic intrusions and the Kanggur–Huangshan ductile shear zone. The rocks in the Hongshi mining area are primarily Lower Carboniferous Gandun Formation rocks and granitoid intrusions (Figs. 2 and 3). The Lower Carboniferous Gandun Formation is divided into two main lithological units: (1) the stratigraphically lower unit, which is composed of tuff, rhyolite, and volcanic breccia with intercalated sandstone and is located in the central and southern mining areas; (2) the upper unit, which is composed of siltstone, sandstone, sandy conglomerate, tuff, and pyroclastic rocks and is located in the northern part of the mining area.

In the southwestern mining area, various granitoid intrusions occur as stocks and dikes, covering an area of approximately 0.8 km² (Fig. 2A). These intrusions intrude into the Lower Carboniferous Gandun Formation and consist of syenogranite, alkali-feldspar granite, and rhyolite porphyry with minor granodiorite (Fig. 2B). Metasedimentary rocks, syenogranite (Fig. 4A), and alkali-feldspar granite (Fig. 4B) are the primary components of the host rocks in the Hongshi gold deposit. In the mining area, the syenogranite and alkali-feldspar granite generally exhibit low or moderate degrees of alteration. The syenogranite is flesh-pink in color and porphyritic in texture; it exhibits a massive structure (Fig. 4C) consisting of K-feldspar (~50%), quartz (~25%), plagioclase (~15%), and biotite (~5%) with accessory magnetite, apatite, and zircon. The K-feldspar is dominated by orthoclase and characterized by a xenomorphic tabular texture. The texture of the quartz is xenomorphic and granular, and some grains exhibit a distinct corroded texture. The plagioclase and biotite are generally hypidiomorphic–xenomorphic. The light-gray alkali-feldspar granite is primarily composed of K-feldspar (~65%), quartz (~25%), and plagioclase (~5%) with accessory
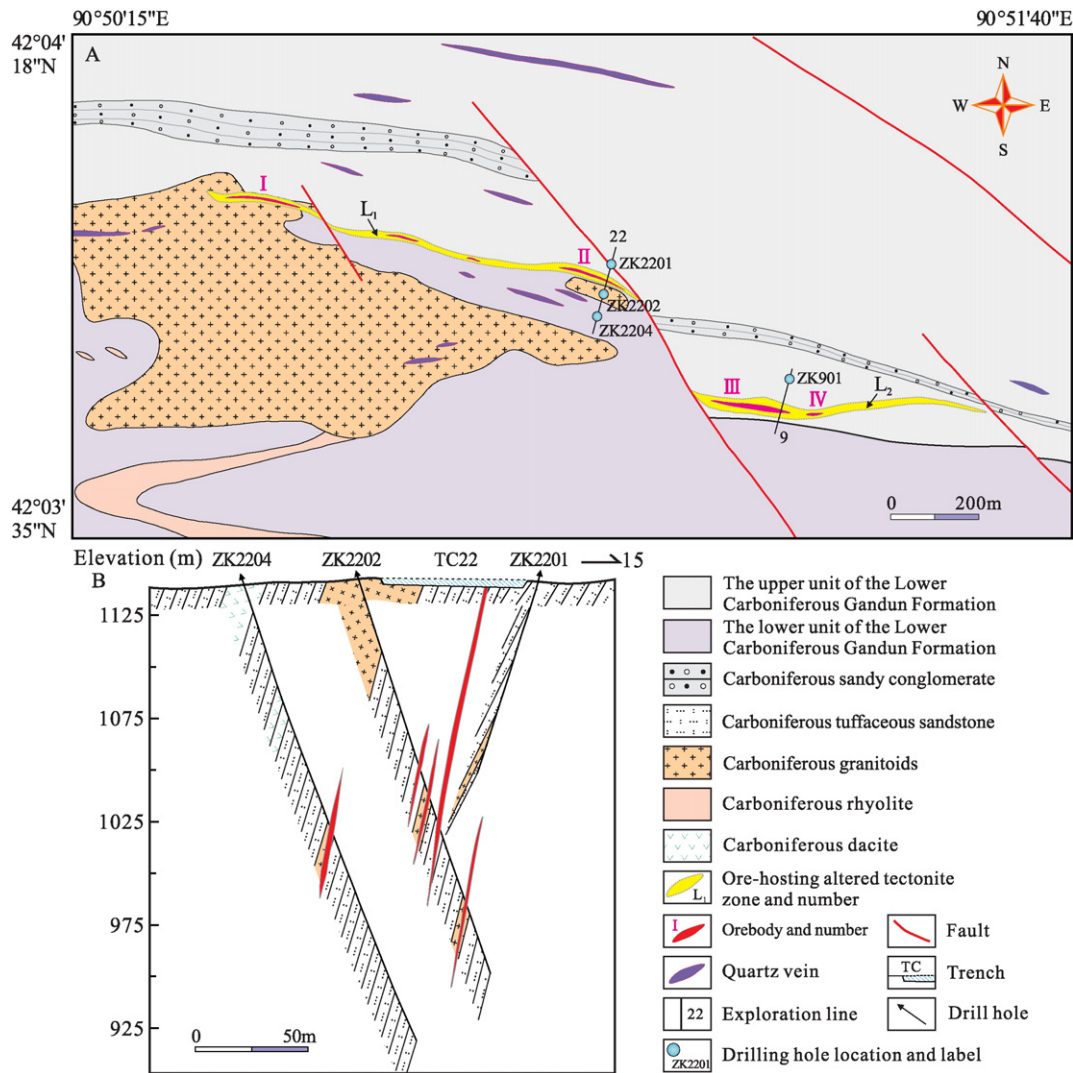
Fig. 2. (A) Simplified map of the Hongshi gold deposit (modified after Sun et al. (2012)). (B) Geological section of the No.22 exploration line across the Hongshi gold deposit (modified from No.1 Geological Party of Xinjiang Bureau of Geology and Mineral Resources (2003)).

apatite and zircon. The K-feldspar is dominated by microcline and is hypidiomorphic–xenomorphic, while the plagioclase is characterized by a hypidiomorphic, tabular texture with polysynthetic twinning (Fig. 4D).

In the Hongshi mining area, the structures are dominated by an EW-trending brittle–ductile shear zone along with a set of conjugate faults trending NW and NWW (Figs. 1C and 2A). As the mining area is a part of the regional giant ductile shear zone striking towards 120° and dipping to 350°–360° (Wang et al., 2007), schistosity is an important structural element. The fault in the mine is characterized by ductile-to-brittle deformation and is primarily composed of mylonitized rocks, mylonites, and schists that grade into moderately deformed rocks with the deformational fabrics developed in mylonitized rocks and mylonites (W.Chen et al., 2007; Wang et al., 2007).

The Hongshi deposit consists of two mineralization belts (L_1 and L_2) with estimated gold resources totaling approximately seven tonnes of Au. The gold mineralization belt L_1 has a strike length of 1100 m, widths varying from 0.47 to 7.65 m, and a down-dip extent of >240 m. Similarly, the mineralization belt L_2 has a strike length of ~700 m, widths varying from 0.37 to 11.32 m, and a down-dip extent of >160 m. These two mineralization belts comprise four gold orebodies (I, II, III, and IV; Fig. 2A) that have thick lenticular surface morphologies. Drill core logging data suggest that the average gold grades L_1 and L_2 are

approximately 6 and 4 g/t, respectively (Sun et al., 2013). Thick auriferous quartz veins and auriferous altered wall rocks dominate the gold mineralization in the Hongshi deposit (Figs. 3, 5A, and B). Native gold, pyrite (Fig. 5C), chalcopyrite (Fig. 5D), galena, sphalerite, siderite, limonite, bornite, and covellite are the primary ore minerals, whereas quartz, calcite, sericite, chlorite, plagioclase, and K-feldspar are the main gangue minerals. The ore occurs as veinlet, stockwork, banded, disseminated, and brecciated structures, while the native gold grains generally occur as inclusions in pyrite crystals or along fissures in pyrite and chlorite (Sun et al., 2013).

Well-developed hydrothermal alteration is observed in the Hongshi gold deposit, and obvious zonation from the orebody to wall rocks occurs. Sericitization, potassic alteration, silification, sulfidation, chloritization, epidote, and carbonate are the main types of alteration. Among these, sericitization is the most spectacular and pervasive; sericite coexists locally with pyrite and other sulfide minerals (Fig. 4E and F). The presence of stockworks and irregular patches of K-feldspar characterizes potassic alteration (Fig. 4E). Silicification occurs mainly in quartz veins and stockworks or in quartz aggregates that coexist with sericite and pyrite (Fig. 4F). Chloritic and epidote alteration are present as replacements of plagioclase and biotite in migmatite of the wall rocks, generally distal to orebodies. Widespread carbonate alteration, locally associated with pyrite, is observed and represents the late-stage evolution of hydrothermal alteration.
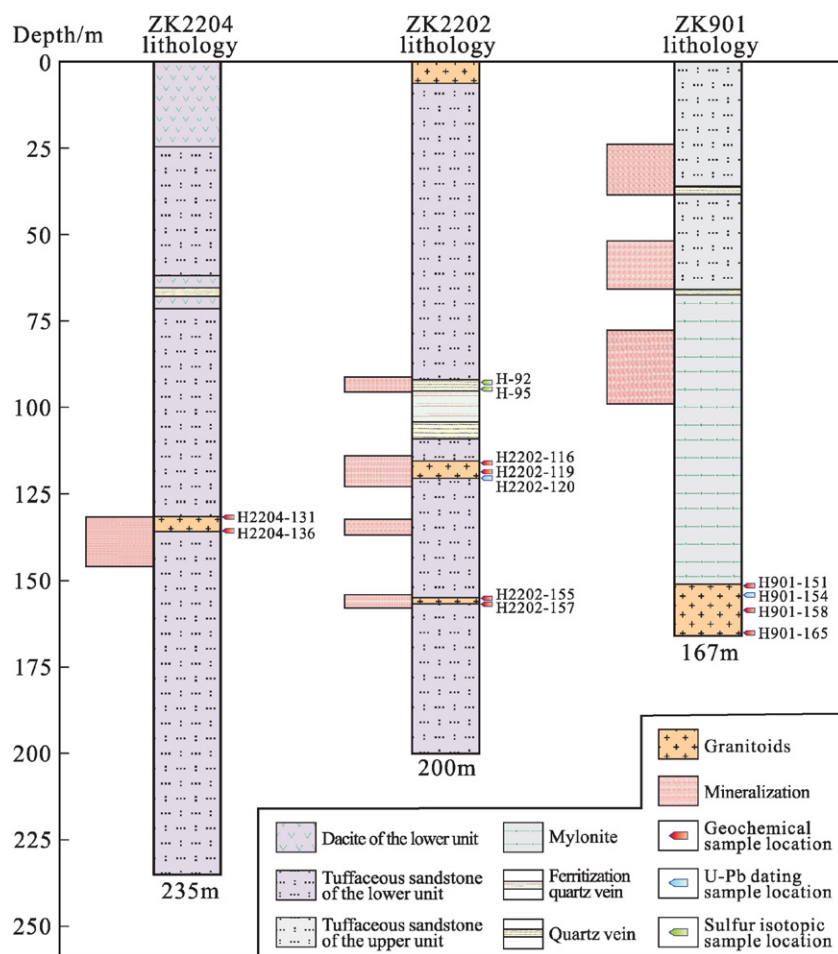
Fig. 3. Histogram of the drilling holes (No. ZK2204, No. ZK2202, and No. ZK901) in the Hongshi gold deposit.

Based on the ore fabrics and mineral assemblages as well as the cross-cutting relationships of veins, three hydrothermal stages can be defined: (I) the first stage is represented by massive quartz accompanied by small amounts of coarse-grained, euhedral-to-subhedral pyrite, with quartz occurring as euhedral grains and exhibiting undulose extinction with minor intracrystalline deformation (Fig. 4G); (II) the second stage, in which the native gold and other sulfide minerals are predominantly formed, is marked by a quartz-polymetallic sulfide assemblage consisting of pyrite, chalcopyrite, galena, and sphalerite (Fig. 4H); (III) the late stage is poor in sulfide + quartz + carbonate (Fig. 4I) and is characterized by the cutting of earlier quartz veins with calcite veinlets.

3. Sampling and analytical techniques

3.1. Sample preparation

Granitoid samples from the Hongshi gold deposit were selected from three drill holes (No. ZK2204, No. ZK2202 and No. ZK901; Fig. 3). The granitoids were variously affected by silicification and sericitization. Therefore, the least-altered samples (i.e., syenogranite and alkali-feldspar granite; locations shown in Fig. 3) were selected for major and trace element, SHRIMP zircon U–Pb, and in situ zircon Hf isotopic analyses to understand their chemical compositions. The dated rocks (H901-154 and H2202-120) were sampled at depths of ~154 and ~120 m, respectively. Moreover, two sulfide samples (H-92 and H-95) were obtained from the main mineralization stage (drill hole No. ZK2202) from depths of 92 and 95 m, respectively, in the Hongshi area for sulfur isotopic analysis (Fig. 3).

3.2. Analytical techniques

The syenogranite and alkali-feldspar granite samples were subjected to whole-rock major and trace element analyses at the Analytical Laboratory of the Beijing Research Institute of Uranium Geology. For the major and trace element analyses, these samples were crushed and powdered to approximately 200 mesh. A Philips PW 2404 X-ray fluorescence (XRF) spectrometer with a rhodium X-ray source was used to determine major elements following the detailed analytical procedures of Norrish and Hutton (1969). The testing precision was better than 1%. Powder samples for trace element analyses were accurately weighed (25 mg) into Savillex Teflon beakers within a high-pressure bomb and then digested in HF + HNO₃ + HClO₄ acid to completely dissolve refractory minerals. An Element-I plasma mass spectrometer (Finnigan-MAT Ltd. German) was used to determine trace elements, including rare earth elements following the analytical procedures of Qi et al. (2000). Analytical quality control was accomplished using national geological standard reference samples GSR-3 and GSR-15, and the analytical precision for trace elements was better than 5%.

Zircon grains were separated from syenogranite and alkali-feldspar granite samples using conventional flotation and electromagnetic techniques followed by handpicking under a binocular microscope at the Langfang Regional Geological Survey in Hebei Province. Cathodoluminescence (CL) images were obtained under an operating power of 15 kV and 4 nA at the electronic probe lab of the Geological Institute of the Chinese Academy of Geological Sciences (CAGS). Using the CL images, the internal structures of the individual zircons were checked, and appropriate spots for zircon
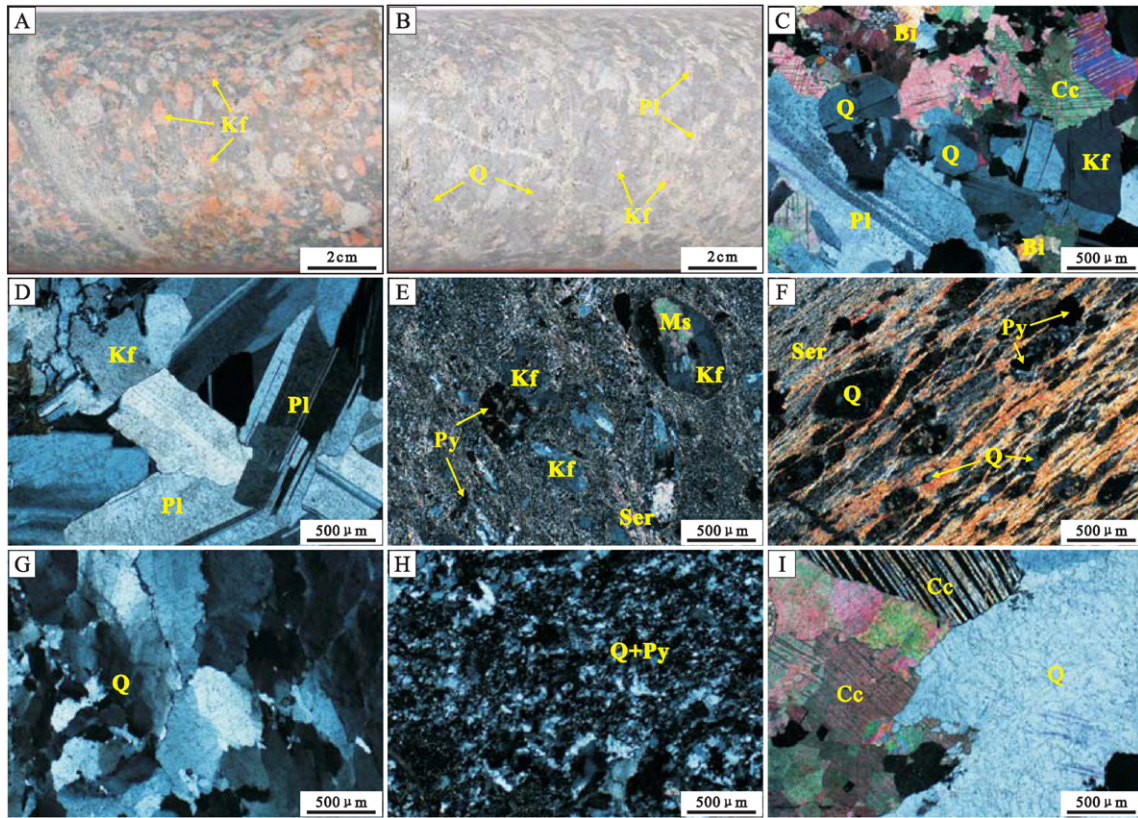
Fig. 4. Photographs and photomicrographs showing the mineralogy of granitoid intrusions and alteration features of the Hongshi gold deposit. (A) Syenogranite. (B) Alkali-feldspar granite. (C) Syenogranite, mainly consisting of K-feldspar, quartz, and plagioclase (crossed polarized light). (D) Alkali-feldspar granite, showing hypidiomorphic tabular plagioclase with polysynthetic twin (crossed polarized light). (E) Altered volcanic rock, showing sericitic and potassic alteration (crossed polarized light). (F) Mylonitization and phyllic alteration assemblage composed of quartz, sericite, and pyrite, associated with the gold mineralization (crossed polarized light). (G) Early-stage quartz with undulose extinction (crossed polarized light). (F) Middle-stage fine-grained quartz associated with pyrite (crossed polarized light). (I) Late-stage carbonatization (crossed polarized light). Abbreviations: Q — quartz; Pl — plagioclase; Kf — K-feldspar; Ser — sericite; Ms. — Muscovite; Cc — calcite; Py — Pyrite.
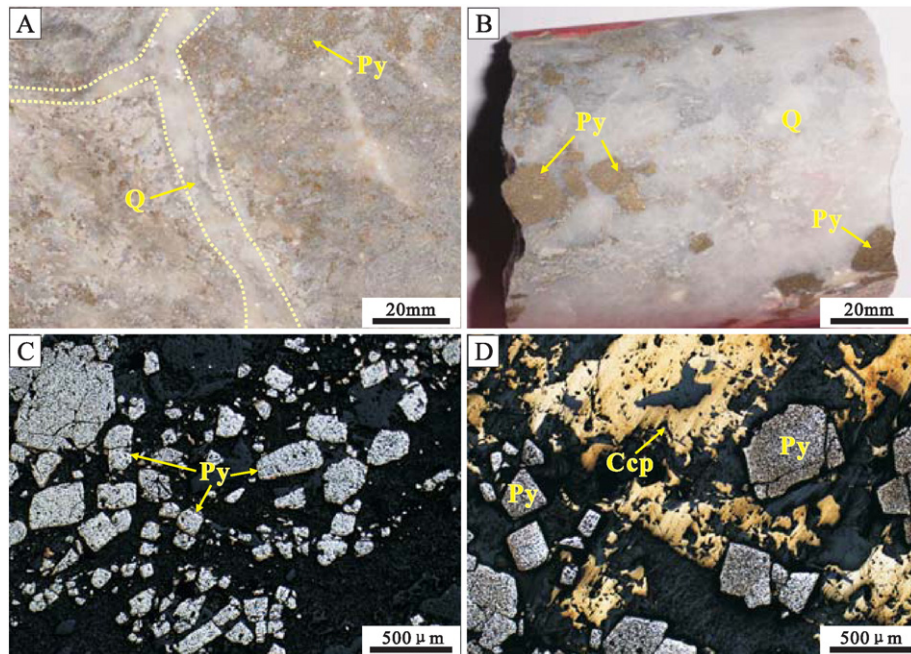

Fig. 5. Photographs and photomicrographs showing the ore fabrics and mineral assemblages of the Hongshi gold deposit: (A) disseminated pyrite in altered rocks; (B) disseminated pyrite in quartz vein; (C) euhedral–subhedral pyrite scattered in quartz vein (reflected light); and (D) brecciated pyrite filled by quartz–chalcopyrite assemblage (reflected light). Abbreviations: Q—quartz; Py—pyrite; Ccp—chalcopyrite.

isotopic analyses were selected. Zircon U–Pb isotopic analyses were performed at the Beijing Ion Probe Center of CAGS using the SHRIMP-II (Sensitive High-Resolution Ion Microprobe) with an ion probe with a spot size of 30 μm. The employed operating conditions were identical to those reported by Liu et al. (2006), and common lead correction was performed using ^{204}Pb with a single testing error of 1σ and a ^{206}Pb/^{238}U weighted average age error of 2σ. The ISOPLOT 3.0 program (Ludwig, 2003) was employed to construct weighted mean U–Pb age and concordia plots.

Using a Neptune MC–ICP–MS and a New Wave UP213 ultraviolet LA–MC–ICP–MS at the Key Laboratory of Metallogeny and Assessment of the Ministry of Land and Resources in CAGS, we conducted in situ zircon Hf isotopic analyses on or close to the spots subjected to U–Pb dating. He was used as the carrier gas to transport the ablated compound through a mixing chamber from the laser–ablation cell to the ICP–MS torch. The ablating diameter was set at 55 or 40 μm depending on the size of the zircon. The employed reference standard was zircon GJ–1 with a weighted mean ^{176}Hf/^{177}Hf ratio of 0.282015 ± 31 (2σ, $n =$

Table 2
Whole-rock geochemical data of Hongshi granitoid intrusions in Eastern Tianshan (major elements: wt.%; trace elements: ppm).

Sample no.	H2204-131	H2204-136	H901-151	H901-158	H901-165	H2202-116	H2202-119	H2202-155	H2202-157
Rock type	Syenogranite	Syenogranite	Syenogranite	Syenogranite	Syenogranite	Alkali-feldspar granite	Alkali-feldspar granite	Alkali-feldspar granite	Alkali-feldspar granite
SiO_2	65.18	65.37	65.39	68.76	69.35	71.67	68.04	68.37	69.29
TiO_2	0.39	0.38	0.39	0.20	0.40	0.31	0.38	0.38	0.37
Al_2O_3	12.75	12.76	12.74	17.27	12.57	12.39	12.51	12.46	12.00
TFe_2O_3	5.02	4.95	5.01	2.47	5.09	3.72	3.92	3.88	3.31
MnO	0.10	0.10	0.10	0.03	0.04	0.04	0.06	0.06	0.01
MgO	0.69	0.71	0.69	1.19	0.46	0.26	0.17	0.17	0.10
CaO	2.78	2.75	2.75	0.43	1.09	0.77	1.96	1.94	0.22
Na_2O	0.22	0.24	0.22	0.68	0.53	0.31	0.26	0.27	0.25
K_2O	9.13	9.08	9.06	6.03	8.53	9.51	10.15	10.00	9.51
P_2O_5	0.08	0.08	0.08	0.04	0.09	0.06	0.07	0.07	0.07
LOI	3.09	3.03	3.02	2.83	1.83	0.95	1.90	1.82	1.82
Total	99.43	99.45	99.44	99.92	99.98	99.99	99.42	99.43	96.95
FeO	1.61	2.09	1.65	0.40	0.75	0.60	1.10	1.24	0.48
A/CNK	0.83	0.84	0.84	2.05	1.04	1.01	0.83	0.84	1.08
A/NK	1.24	1.24	1.25	2.25	1.24	1.14	1.09	1.10	1.12
Mg#	22	22	22	49	15	12	8	8	6
Li	8.66	9.12	8.67	38.6	5.29	3.28	2.43	2.82	1.35
Be	0.666	0.578	1.15	2.71	0.868	0.679	0.592	0.661	0.676
Sc	16.5	16	16.2	7.76	25.7	16.6	11.6	12.5	12.6
V	114	113	110	33.5	103	67.1	98.7	108	86.2
Cr	100	118	78.1	4.86	73	21.7	203	230	131
Co	8.5	8.2	7.7	7.81	9.38	5.14	11.9	12.3	8.24
Ni	8.33	7.73	7.77	3.57	8.03	4.96	8.94	9.23	5.01
Cu	59.2	65.5	64.7	36.4	45.9	19.1	23.6	26.5	169
Zn	48.4	47.7	46.7	38.5	24.9	18.3	21.2	22.3	68.7
Ga	14.1	13.3	13	17.3	12.9	9.65	10.4	11.1	10
Rb	301	293	291	272	285	281	322	350	247
Sr	82	77.8	77.8	41.4	96	58.9	57.8	62.4	76.8
Y	15	14.5	14.4	25.7	12.8	11.2	15.9	17.2	12.3
Zr	107	113	99.9	152	121	119	128	118	104
Nb	4.74	4.87	4.68	9.61	4.7	4.87	5.4	5.82	5.28
Cs	8.82	8.52	8.56	23.3	2.85	3.23	3.15	3.36	1.97
Ba	2471	2309	2336	3364	1144	1610	1478	1509	9853
La	16.3	13	12.8	25.8	6.89	12.3	11.4	12.1	10.7
Ce	30.5	25.4	24.5	56.1	14.4	24.7	23.1	24.4	19.4
Pr	3.45	2.91	2.81	6.13	1.68	2.79	2.67	2.88	2.22
Nd	13	11.6	11.3	23.3	7.13	10.2	10.6	11.1	8.64
Sm	2.45	2.34	2.24	4.84	1.81	1.9	2.26	2.49	1.79
Eu	0.748	0.782	0.673	1.56	0.721	0.672	0.624	0.82	0.471
Gd	2.71	2.8	2.62	4.52	1.91	1.7	2.32	2.46	1.97
Tb	0.412	0.452	0.414	0.818	0.372	0.304	0.457	0.517	0.373
Dy	2.57	2.57	2.35	5.03	2.39	1.99	2.75	3.1	2.11
Ho	0.488	0.537	0.517	0.958	0.48	0.411	0.55	0.665	0.436
Er	1.42	1.27	1.32	2.99	1.57	1.42	1.69	1.8	1.3
Tm	0.242	0.248	0.25	0.492	0.277	0.246	0.257	0.289	0.235
Yb	1.53	1.54	1.56	3.31	1.77	1.66	1.66	1.59	1.43
Lu	0.309	0.325	0.285	0.516	0.297	0.291	0.335	0.33	0.279
Hf	3.15	3.45	3.07	4.93	3.42	3.47	3.63	3.51	2.64
Ta	0.461	0.421	0.427	0.988	0.511	0.55	0.448	0.529	0.473
Pb	4.34	4.12	4.24	4.43	16	5.1	6.86	7.23	5.41
Th	5.16	4.9	4.9	11.1	6.11	6.94	5.84	6.43	5.29
U	1.31	1.25	1.27	1.73	1.55	1.59	1.37	1.51	1.54
LREE/HREE	9.92	8.47	8.50	8.66	4.83	8.58	6.88	6.78	7.33
$(La/Yb)_N$	7.64	6.06	5.89	5.59	2.79	5.31	4.93	5.46	5.37
Sr/Y	5.47	5.37	5.40	1.61	7.50	5.26	3.64	3.63	6.24
Nb/Ta	10.28	11.57	10.96	9.73	9.20	8.85	12.05	11.00	11.16
Eu/Eu*	0.89	0.93	0.85	1.02	1.19	1.14	0.83	1.01	0.77

LOI = loss on ignition. A/CNK = molecular $Al_2O_3/(CaO + Na_2O + K_2O)$; A/NK = molecular $Al_2O_3/(Na_2O + K_2O)$. Mg# = $100 \times$ molar $Mg^{2+}/(Mg^{2+} + Fe^{2+})$, calculated by assuming $TFeO = 0.9 \times TFe_2O_3$. Eu/Eu* = $Eu_N/(Sm_N \times Gd_N)^{1/2}$, the subscript of N means normalized to chondrite (Sun and McDonough, 1989).

10). The employed instrumental conditions and data acquisition procedures are detailed in Wu et al. (2006) and Hou et al. (2007), and all Lu–Hf isotopic analysis results are reported with an error of 2σ. The ^{176}Lu decay constant of Soderlund et al. (2004) (1.867 × 10^{-11} year^{-1}) was adopted, and the initial Hf isotope ratios and ε$_{Hf}$(t) values were calculated using the chondritic reservoir at the time of zircon growth from magma as a reference. The depleted mantle model ages (T$_{DM}$) were calculated with respect to the depleted mantle using a present-day ^{176}Hf/^{177}Hf of 0.28325 and a ^{176}Lu/^{177}Hf value of 0.0384 (Griffin et al., 2002). The zircon Hf isotope crustal model ages (T$_{DM}$^{c}) were calculated with respect to the average continental crust assuming ^{176}Lu/^{177}Hf = 0.015 (Griffin et al., 2002).

The sulfide minerals were separated via flotation and electromagnetic methods at the Langfang Regional Geological Survey in Hebei Province. Sulfur isotopes were analyzed using a Finnigan MAT 251EM mass spectrometer at the Analytical Laboratory of the Beijing Research Institute of Uranium Geology, and the δ^{34}S of sulfide was determined on SO$_2$ obtained by placing the sulfide–CuO composite (with a weight ratio of 1/7) into a vacuum system heated to 980 °C. Isotopic data were reported relative to the Canyon Diablo Triolite (CDT) standard for δ^{34}S, and the analytic precision was ±0.2‰ for δ^{34}S.

4. Results

4.1. Whole-rock geochemistry

Table 2 presents the whole-rock geochemical data of nine representative samples from the Hongshi deposit. The granitoid samples plot within the syenogranite and alkali-feldspar granite fields of the quartz-alkali feldspar-plagioclase (QAP) diagram (Fig. 6A). These granitoids have SiO$_2$ contents ranging from 65.18 to 71.67 wt.%, and all granitoid samples recorded Al$_2$O$_3$ contents greater than 12 wt.% along with low contents of Na$_2$O (0.22–0.68 wt.%), MgO (0.10–1.19 wt.%), MnO (0.01–0.10 wt.%), TiO$_2$ (0.20–0.40 wt.%), and P$_2$O$_5$ (0.04–0.09 wt.%). With the exception of sample H901-158, the A/CNK values of the samples (Al$_2$O$_3$/[CaO + Na$_2$O + K$_2$O], mole ratio) range from 0.83 to 1.08, indicative of a metaluminous to weakly peraluminous composition (Fig. 6B). The granitoid samples plot in the field of the shoshonitic series (Fig. 7A) with high K$_2$O contents (6.03–10.15 wt.%), and with the exception of one sample, they recorded slightly low Mg$^\#$ values of 6–22 (Table 2). The Harker diagrams of major elements show that the P$_2$O$_5$, CaO, MnO, and Fe$_2$O$_3^T$ contents of the Hongshi granitoids are negatively correlated with SiO$_2$ content, whereas the Na$_2$O and Al$_2$O$_3$ contents show no clear correlation with SiO$_2$ content (Fig. 7B–H).

The rare earth element (REE) and trace element patterns of the Hongshi granitoid samples are similar (Fig. 8). The chondrite-normalized REE diagrams (Fig. 8A; Boynton, 1984) indicate that the granitoids are moderately enriched in light rare earth elements (LREEs) and relatively depleted in heavy rare earth elements (HREEs) ((La/Yb)$_N$ = 2.79–7.64) without any significant Eu anomaly (Eu/Eu* = 0.77–1.19; Table 2). The primitive mantle-normalized trace element pattern (Fig. 8B; Sun and McDonough, 1989) suggests that the rocks are strongly enriched in large-ion lithophile elements (LILEs) such as Rb, K, Ba, and Pb, whereas they are markedly depleted in high field strength elements (HFSEs) such as Nb, Ta, P, and Ti.

4.2. SHRIMP zircon U–Pb dating

SHRIMP zircon U–Pb dating was performed on syenogranite (H901-154) and alkali-feldspar granite (H2202-120) samples from the Hongshi gold deposit, and the results are presented in Table 3. The zircon grains of the two granitoid samples are euhedral to subhedral, colorless, and mainly prismatic in shape, with length/width ratios of approximately 2:1 to 4:1. The CL images of the analyzed zircon grains display clear oscillatory zoning with homogeneous cores (Fig. 9A and B). The ^{238}U and ^{232}Th contents of the grains ranged from 131 to 588 and from 72 to 670 ppm, respectively, and their Th/U ratios were high (0.42–1.18; Table 3). Fig. 9 shows the CL images of the analyzed zircons along with the concordia diagrams.

Fifteen spots on the zircons from the Hongshi syenogranite sample (H901-154) were analyzed. With the exception of one discordant spot with high common Pb (H901-154-5), the remaining fourteen analyses gave ^{206}Pb/^{238}U ages ranging from 321.9 ± 6.3 to 347.8 ± 6.9 Ma, corresponding to a weighted mean ^{206}Pb/^{238}U age of 337.6 ± 4.5 Ma (2σ, MSWD = 1.3; Fig. 9C); this age is considered to record the emplacement age of this intrusion. Thirteen spots were analyzed on the zircons of the Hongshi alkali-feldspar granite sample (H2202-120). All spots except for one (H2202-120-4) gave ^{206}Pb/^{238}U ages ranging from 321.4 ± 6.2 to 347.6 ± 6.9 Ma. These ages correspond to a weighted mean ^{206}Pb/^{238}U age of 334.0 ± 3.7 Ma (2σ, MSWD = 1.1; Fig. 9D), which is interpreted as the time of crystallization of this intrusion.

4.3. Zircon Hf isotopes

Fig. 9A and B shows the in situ Hf isotopic analyses of zircons from the syenogranite (H901-154) and alkali-feldspar granite (H2202-120) samples, respectively. The zircon Hf isotopic data and calculation results are presented in Table 4 and Fig. 10. The syenogranite magmatic zircons with crystallization ages of 337.6 Ma exhibit variable ^{176}Hf/^{177}Hf ratios
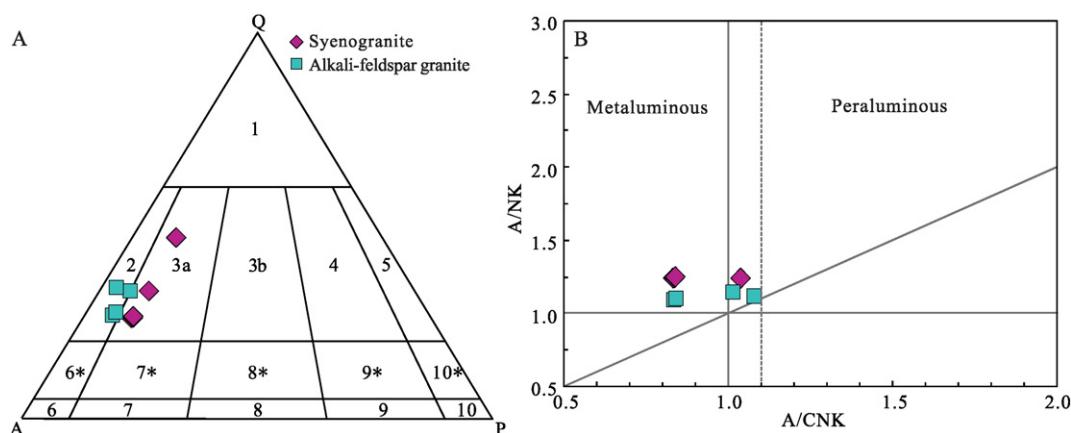

Fig. 6. Classification and diagrams of granitoid intrusions in the Hongshi gold deposit: (A) QAP modal diagram (Le Maitre, 1989) and (B) A/NK vs. A/CNK plot (Maniar and Piccoli, 1989). Q. quartz; A. alkali-feldspar; P. plagioclase; (1) quartz-rich granite; (2) alkali-feldspar granite; (3a) granite (syenogranite); (3b) granite (monzogranite); (4) granodiorite; (5) tonalite and plagiogranite; (6*) alkali-feldspar quartz syenite; (7*) quartz syenite; (8*) quartz mononite; (9*) quartz monzodiorite; (10*) quartz diorite; (6) alkali-feldspar syenite; (7) syenite; (8) monzonite; (9) monzodiorite, monzogabbro; and (10) diorite, gabbro, anorthosite. A/NK = molecular Al$_2$O$_3$/(Na$_2$O + K$_2$O); A/CNK = molecular Al$_2$O$_3$/(CaO + Na$_2$O + K$_2$O).
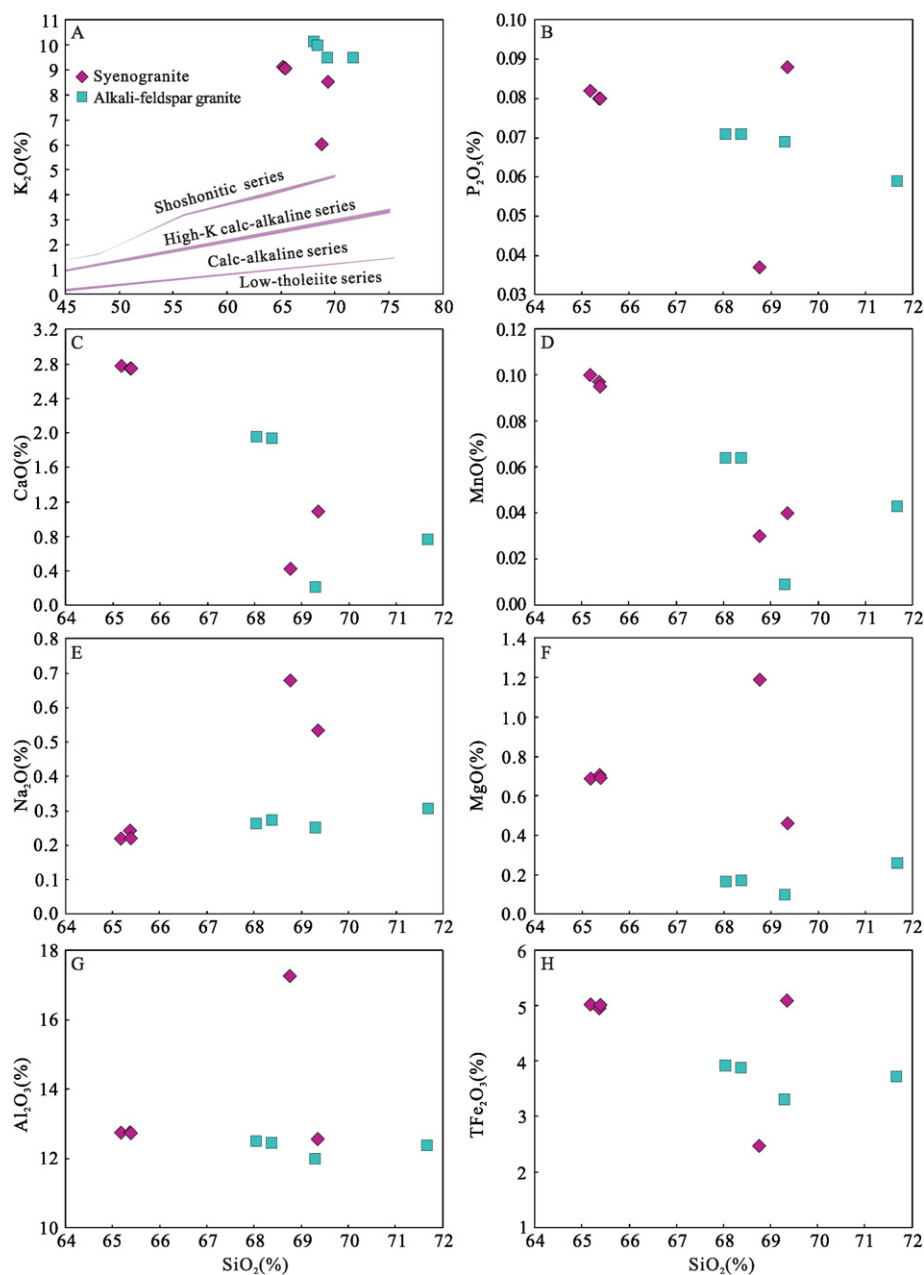
Fig. 7. Harker diagram of granitoid intrusions in the Hongshi gold deposit.
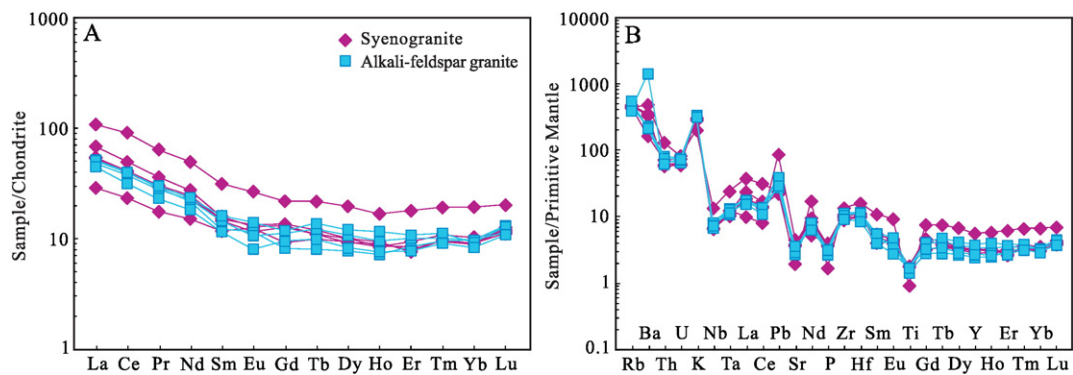

Fig. 8. Chondrite-normalized REE (A) and primitive mantle-normalized trace element abundance spider diagram (B) for Hongshi granitoid intrusions (normalized data are from Boynton (1984) and Sun and McDonough (1989)).

Table 3
SHRIMP zircon U–Pb data of the Hongshi granitoid intrusions in Eastern Tianshan.

Spot	$^{206}Pb_c$/%	U/ppm	Th/ppm	Th/U	$^{206}Pb^*$/ppm	Isotopic ratios								$^{206}Pb/^{238}U$	±1σ
						$^{238}U/^{206}Pb^*$	±1σ	$^{207}Pb^*/^{206}Pb^*$	±1σ	$^{207}Pb^*/^{235}U$	±1σ	$^{206}Pb^*/^{238}U$	±1σ		
H901-154, syenogranite, 14 spots (without spot 5), weighted mean age = 337.6 ± 4.5 Ma, MSWD = 1.3															
H901-154-1	0.95	189	98	0.54	8.84	18.5438	0.0202	0.0457	0.0426	0.3398	0.0471	0.0539	0.0202	338.6	6.7
H901-154-2	0.24	183	84	0.47	8.69	18.1340	0.0206	0.0564	0.0267	0.4289	0.0337	0.0551	0.0206	346.0	6.9
H901-154-3	0.47	166	72	0.45	7.58	18.8530	0.0244	0.0492	0.0396	0.3595	0.0465	0.0530	0.0244	333.2	7.9
H901-154-4	0.43	184	87	0.49	8.59	18.4416	0.0201	0.0492	0.0277	0.3679	0.0343	0.0542	0.0201	340.4	6.7
H901-154-5	1.48	150	77	0.53	7.69	17.0119	0.0209	0.0489	0.0759	0.3960	0.0787	0.0588	0.0209	368.2	7.5
H901-154-6	0.14	211	110	0.54	9.83	18.4347	0.0199	0.0515	0.0222	0.3855	0.0298	0.0542	0.0199	340.5	6.6
H901-154-7	0.64	150	97	0.67	7.09	18.3258	0.0203	0.0456	0.0361	0.3428	0.0414	0.0546	0.0203	342.5	6.8
H901-154-8	0.40	228	149	0.67	10.80	18.2048	0.0199	0.0523	0.0271	0.3965	0.0336	0.0549	0.0199	344.7	6.7
H901-154-9	0.31	238	140	0.61	11.20	18.3715	0.0199	0.0509	0.0241	0.3818	0.0312	0.0544	0.0199	341.7	6.6
H901-154-10	0.18	302	155	0.53	13.80	18.7890	0.0197	0.0527	0.0188	0.3870	0.0272	0.0532	0.0197	334.3	6.4
H901-154-11	0.25	145	79	0.56	6.47	19.2621	0.0204	0.0522	0.0268	0.3735	0.0337	0.0519	0.0204	326.3	6.5
H901-154-12	1.54	157	77	0.51	7.22	19.0146	0.0209	0.0458	0.0980	0.3322	0.1002	0.0526	0.0209	330.4	6.7
H901-154-13	0.46	234	128	0.56	10.40	19.5273	0.0199	0.0508	0.0277	0.3588	0.0341	0.0512	0.0199	321.9	6.3
H901-154-14	1.07	210	103	0.50	10.10	18.0371	0.0202	0.0464	0.0617	0.3551	0.0650	0.0554	0.0202	347.8	6.9
H901-154-15	0.66	201	98	0.51	9.44	18.3819	0.0201	0.0480	0.0398	0.3601	0.0446	0.0544	0.0201	341.5	6.7
H2202-120, alkali-feldspar granite, 12 spots (without spot 4), weighted mean age = 334.0 ± 3.7 Ma, MSWD = 1.1															
H2202-120-1	0.38	302	122	0.42	13.60	19.1094	0.0199	0.0499	0.0307	0.3598	0.0366	0.0523	0.0199	328.8	6.4
H2202-120-2	0.32	171	106	0.64	7.98	18.4534	0.0205	0.0511	0.0274	0.3819	0.0342	0.0542	0.0205	340.2	6.8
H2202-120-3	0.15	588	670	1.18	27.00	18.7708	0.0196	0.0515	0.0201	0.3786	0.0280	0.0533	0.0196	334.6	6.4
H2202-120-4	0.42	162	92	0.59	8.01	17.4462	0.0205	0.0492	0.0369	0.3887	0.0422	0.0573	0.0205	359.3	7.2
H2202-120-5	0.23	422	323	0.79	19.50	18.6071	0.0196	0.0498	0.0208	0.3692	0.0286	0.0537	0.0196	337.5	6.5
H2202-120-6	0.14	281	136	0.50	12.80	18.8383	0.0200	0.0513	0.0221	0.3757	0.0298	0.0531	0.0200	333.4	6.5
H2202-120-7	0.34	167	96	0.60	7.96	18.0485	0.0205	0.0542	0.0317	0.4138	0.0378	0.0554	0.0205	347.6	6.9
H2202-120-8	0.19	192	124	0.67	8.99	18.4047	0.0218	0.0553	0.0381	0.4142	0.0439	0.0543	0.0218	341.1	7.2
H2202-120-9	0.48	131	73	0.57	6.05	18.7321	0.0213	0.0489	0.0391	0.3599	0.0445	0.0534	0.0213	335.3	7.0
H2202-120-10	0.59	173	99	0.59	7.75	19.2651	0.0205	0.0511	0.0461	0.3658	0.0504	0.0519	0.0205	326.2	6.5
H2202-120-11	0.34	294	250	0.88	13.40	18.8348	0.0209	0.0515	0.0244	0.3772	0.0321	0.0531	0.0209	333.5	6.8
H2202-120-12	0.19	360	246	0.71	15.80	19.5611	0.0197	0.0531	0.0195	0.3744	0.0277	0.0511	0.0197	321.4	6.2
H2202-120-13	0.53	210	157	0.77	9.61	18.8519	0.0201	0.0499	0.0395	0.3650	0.0443	0.0530	0.0201	333.2	6.5

ranging from 0.282620 to 0.282837 as well as positive $\varepsilon_{Hf}(t)$ values between $+1.5$ and $+8.8$ (Fig. 10B), with an average value of $+5.6$. The corresponding Hf depleted model ages (T_{DM}) vary from 653 to 917 Ma, and the crustal model ages (T^C_{DM}) range from 788 to 1244 Ma (Fig. 10C). The $^{176}Hf/^{177}Hf$ ratios of the alkali-feldspar magmatic zircons with crystallization ages of 334.0 Ma vary from 0.282707 to 0.282868, and their $\varepsilon_{Hf}(t)$ values are positive, ranging from $+5.0$ to $+10.1$ (Fig. 10B) with an average of $+7.9$. The corresponding Hf depleted model ages (T_{DM}) range from 577 to 785 Ma, while the crustal model ages (T^C_{DM}) vary from 698 to 1035 Ma (Fig. 10C); these values are slightly lower than those of the syenogranite zircons.

4.4. Sulfur isotopes

Table 5 and Fig. 11B show the sulfur isotopic compositions of the two Hongshi gold deposit sulfide samples along with some previous data. The ten sulfide samples exhibit $\delta^{34}S$ values ranging from $-11.5‰$ to $+4.2‰$, with most values concentrated between $+1‰$ and $+4‰$. These $\delta^{34}S$ values suggest that the Hongshi gold deposit has sulfur isotopic characteristics similar to most orogenic gold deposits in the Chinese Tianshan Orogenic belt, such as the Kanggur, Awanda, and Jinwozi deposits (Ding et al., 2014; Wang et al., 2015c).

5. Discussion

5.1. Magma source and petrogenesis

The petrochemical signatures of magmatic rocks provide valuable information regarding the location of the magma source, magmatic process, and the tectonic setting (Barbarin, 1999; Mo et al., 2009; Sylvester, 1998; Wang et al., 2015b, 2015e; Zhu et al., 2013). For this reason, it is important to develop a clear understanding of the petrogenetic history of the Hongshi granitoid intrusions. The Hongshi granitoid samples are characterized by high SiO_2 (65.18–71.67 wt.%) and K_2O (6.03–10.15 wt.%) contents accompanied by relatively low A/CNK values (mostly <1.1). Although some plots of P_2O_5, CaO, MnO, and $Fe_2O_3^T$ indicate negative correlations with SiO_2 content, the Harker diagrams of major elements generally show that Na_2O and Al_2O_3 plot outside of the systematic fractional crystallization trend, with no clear correlation with SiO_2 content (Fig. 7). These features suggest that the primary magmas of the Hongshi granitoid intrusions share the same source with some contributions from the partial mixing of other materials (Li et al., 2015).

Regardless of melting degree, melts from the lower crust are generally characterized by low Mg# values (<40); Mg# exceeding 40 is only found when mantle materials are involved (Rapp and Watson, 1995). The majority of the Hongshi granitoids have relatively low MgO contents ranging from 0.10 to 0.71% and Mg# values between 6 and 22, similar to those of melts derived from the juvenile thickened lower crust. One syenogranite sample (H901-158) exhibited higher MgO and Mg# values (Mg# = 49), which are attributed to partial mixing with mantle-derived materials.

The samples show uniform REE and trace element abundances and patterns, which are markedly enriched in LILEs, and exhibit strong negative anomalies of Nb, Ta, P, and Ti (Fig. 8). Both the LREE/HREE values (4.83–9.92) and the slight Eu anomalies (Eu/Eu* = 0.77–1.19) suggest that plagioclase melting occurred in the source (Li et al., 2015). The Nb/Ta ratios of the granitoids range from 8.85 to 12.05 with an average of 10.53, consistent with those of crustal rocks (11–12; Green, 1995).
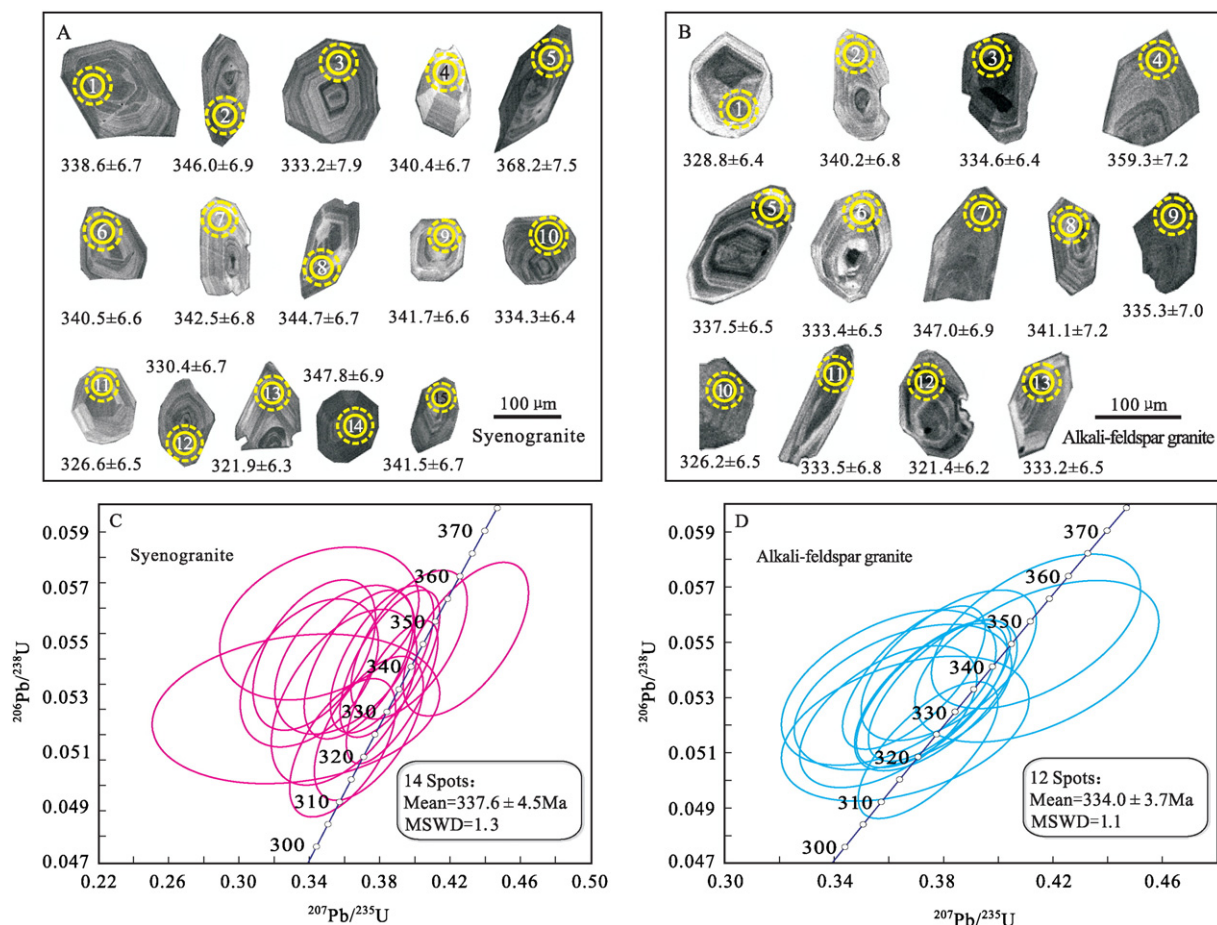

Fig. 9. Cathodoluminescence images (A, B) and concordia plots (C, D) of zircons from syenogranite and alkali-feldspar granite in the Hongshi gold deposit.

The Sr concentrations (41.4–96.0 ppm) and Sr/Y values (1.61–7.50) of the granitoids are significantly low, comparable to those of normal arc rocks (Tatsumi and Eggins, 1995). The above characteristics provide further evidence that the Hongshi granitoids were not formed by the melting of subducted oceanic-slab followed by the interaction with continental crust; instead, the mixing of the juvenile lower crust-derived melts with some mantle materials may explain their formation.

The $^{176}Hf/^{177}Hf$ ratios of zircons from the granitoids ranged from 0.282620 to 0.282868, indicating primarily homogeneous Hf isotopic compositions, which are typical of grains of magmatic origin. The $\varepsilon_{Hf}(t)$ values vary from + 1.5 to + 10.1; the corresponding Hf depleted model ages (T_{DM}) ranged from 577 Ma to 917 Ma, while the Hf crustal model ages (T^C_{DM}) were between 698 Ma and 1244 Ma (Fig. 10). These values suggest a juvenile lower crust as the primary magma of these granitoids. The $\varepsilon_{Hf}(t)$ values of the Hongshi granitoid zircons were inhomogeneous, with variations of as much as 8.6ε (Table 3). This suggests that the Hongshi granitoid intrusions likely derived from the melting of juvenile lower crust that mixed with some mantle-derived materials.

5.2. Source of ore fluids and metals

At Hongshi, the fluid inclusions in auriferous quartz veins are dominated by H_2O–CO_2 and have high CO_2 contents (Wang et al., 2007; Zhang et al., 2012). The ore fluid is characterized by low salinity (1.05–10.73 wt.% NaCl eqv.) and moderate-to-low temperature (113 °C–353 °C), as demonstrated by microthermometric

measurements(Wang et al., 2007). These values are similar to those of orogenic-type deposits (Deng et al., 2015a, 2015b). As indicated by the available oxygen and hydrogen isotope data, the ore fluids from different mineralization stages exhibit $\delta^{18}O$ values ranging from − 1.7‰ to + 7.4‰ and δD_w values from − 104‰ to − 63‰ (Wang et al., 2007; Zhang et al., 2012). Due to the variable $\delta^{18}O_w$ values, the data points corresponding to mineralization stages I to III in the $\delta^{18}O_w$ versus δD_w diagram extend from the metamorphic and magmatic water regions to the meteoric water line (Fig. 11A). This suggests that the primary source of the Hongshi deposit fluids was metamorphic fluid generated by sedimentary rocks containing organic matter.

The CH_4 gas extracted from the Hongshi auriferous quartz exhibited $\delta^{13}C$ values ranging from − 28.8‰ to − 23.8‰ with an average of − 26.2‰ (Table 5; L.J. Wang et al., 2006). As this average value is close to − 25‰, the source of the CH_4 gas is considered to be a biogenic hydrocarbons. Two relatively low $\delta^{13}C_{CH4}$ values (− 28.8‰ and − 28.2‰) suggest a contribution from sedimentary organic carbon (Giggenbach, 1995; Shen et al., 2015). Carbon-bearing host rocks are found in the Lower Carboniferous Gandun Formation in the Hongshi area. These host rocks include carbonaceous tuffaceous sandstone and limestone; thus, the CH_4 was possibly generated from these carbon-bearing host rocks. The CO_2 gas formed in the Hongshi auriferous quartz exhibits a wide range of $\delta^{13}C$ values (− 11.6‰ to − 5.2 ‰ with an average of − 7.5‰; Table 5). These values suggest that the CO_2 was not derived from a single source, and that the carbon isotopes were not homogenized within the ore fluid. Two relatively low $\delta^{13}C_{CO2}$ values were observed (− 11.6‰ and − 10.1 ‰); these values are comparable

Table 4
Zircon Hf isotopic data of the Hongshi granitoid intrusions in Eastern Tianshan.

Spot	Age/Ma	$^{176}Yb/^{177}Hf$	$^{176}Lu/^{177}Hf$	$^{176}Hf/^{177}Hf$	± 2σ	$^{176}Hf/^{177}Hf$(t)	$^{176}Hf/^{177}Hf$ CHUR(t)	$\varepsilon_{Hf}(0)$	$\varepsilon_{Hf}(t)$	T_{DM}/Ma	$T_{DM}{}^C$/Ma	$f_{Lu/Hf}$
H901-154, syenogranite, 337.6 ± 4.5 Ma, $\varepsilon_{Hf}(t) = +1.5 \sim +8.8$ (15 spots)												
H901-154-1	338.6	0.120758	0.002048	0.282720	0.000027	0.282707	0.282561	− 1.9	5.1	776	1018	− 0.94
H901-154-2	346.0	0.121293	0.002023	0.282743	0.000025	0.282730	0.282557	− 1.0	6.1	741	960	− 0.94
H901-154-3	333.2	0.117224	0.001922	0.282620	0.000028	0.282608	0.282565	− 5.4	1.5	917	1244	− 0.94
H901-154-4	340.4	0.121981	0.001934	0.282689	0.000026	0.282677	0.282560	− 2.9	4.1	818	1084	− 0.94
H901-154-5	368.2	0.093100	0.001685	0.282695	0.000021	0.282684	0.282543	− 2.7	5.0	803	1050	− 0.95
H901-154-6	340.5	0.123546	0.002241	0.282646	0.000021	0.282631	0.282560	− 4.5	2.5	888	1186	− 0.93
H901-154-7	342.5	0.120071	0.002099	0.282767	0.000021	0.282754	0.282559	− 0.2	6.9	707	908	− 0.94
H901-154-8	344.7	0.248694	0.004758	0.282837	0.000029	0.282807	0.282558	2.3	8.8	653	788	− 0.86
H901-154-9	341.7	0.169214	0.003786	0.282793	0.000031	0.282769	0.282560	0.7	7.4	703	876	− 0.89
H901-154-10	334.3	0.121761	0.002061	0.282692	0.000024	0.282679	0.282564	− 2.8	4.1	816	1082	− 0.94
H901-154-11	326.3	0.151223	0.002349	0.282727	0.000029	0.282712	0.282569	− 1.6	5.1	772	1013	− 0.93
H901-154-12	330.4	0.103858	0.001776	0.282754	0.000025	0.282743	0.282567	− 0.6	6.3	720	940	− 0.95
H901-154-13	321.9	0.213274	0.004223	0.282783	0.000031	0.282758	0.282572	0.4	6.6	727	913	− 0.87
H901-154-14	347.8	0.167849	0.003364	0.282801	0.000023	0.282779	0.282556	1.0	7.9	683	849	− 0.90
H901-154-15	341.5	0.226172	0.005111	0.282793	0.000037	0.282760	0.282560	0.7	7.1	730	895	− 0.85
H2202-120, alkali-feldspar granite, 334.0 ± 3.7 Ma, $\varepsilon_{Hf}(t) = +5.0 \sim +10.1$ (13 spots)												
H2202-120-1	328.8	0.227092	0.003644	0.282824	0.000031	0.282802	0.282568	1.9	8.3	652	809	− 0.89
H2202-120-2	340.2	0.113864	0.001932	0.282814	0.000024	0.282802	0.282560	1.5	8.5	636	801	− 0.94
H2202-120-3	334.6	0.213745	0.003627	0.282830	0.000025	0.282808	0.282564	2.1	8.6	643	792	− 0.89
H2202-120-4	359.3	0.082855	0.001359	0.282776	0.000024	0.282767	0.282549	0.2	7.7	681	868	− 0.96
H2202-120-5	337.5	0.173341	0.003081	0.282868	0.000033	0.282848	0.282562	3.4	10.1	577	698	− 0.91
H2202-120-6	333.4	0.136824	0.002752	0.282791	0.000019	0.282774	0.282565	0.7	7.4	685	869	− 0.92
H2202-120-7	347.6	0.087745	0.001657	0.282707	0.000020	0.282697	0.282556	− 2.3	5.0	785	1035	− 0.95
H2202-120-8	341.1	0.204452	0.004494	0.282848	0.000027	0.282819	0.282560	2.7	9.2	632	763	− 0.86
H2202-120-9	335.3	0.112442	0.002493	0.282754	0.000021	0.282738	0.282564	− 0.7	6.2	736	949	− 0.92
H2202-120-10	326.2	0.237153	0.005339	0.282793	0.000038	0.282761	0.282569	0.7	6.8	735	904	− 0.84
H2202-120-11	333.5	0.250965	0.004598	0.282835	0.000030	0.282806	0.282565	2.2	8.5	654	797	− 0.86
H2202-120-12	321.4	0.241800	0.004877	0.282785	0.000033	0.282755	0.282572	0.5	6.5	738	918	− 0.85
H2202-120-13	333.2	0.200719	0.003980	0.282854	0.000030	0.282829	0.282565	2.9	9.3	613	745	− 0.88

$\varepsilon_{Hf}(t) = 10000 \times (\{[(^{176}Hf/^{177}Hf)_S - (^{176}Lu/^{177}Hf)_S \times (e^{\lambda t} - 1)]/[(^{176}Hf/^{177}Hf)_{CHUR,0} - (^{176}Lu/^{177}Hf)_{CHUR} \times ((e^{\lambda t} - 1)] - 1\}$.

$T_{DM} = 1/\lambda \times \ln\{1 + [(^{176}Hf/^{177}Hf)_S - (^{176}Hf/^{177}Hf)_{DM}]/[(^{176}Lu/^{177}Hf)_S - (^{176}Lu/^{177}Hf)_{DM}]\}$.

$T_{DM}{}^C = T_{DM} - (T_{DM} - t) \times [(f_{cc} - f_s)/(f_{cc} - f_{DM})]$.

$f_{Lu/Hf} = (^{176}Lu/^{177}Hf)_S/(^{176}Lu/^{177}Hf)_{CHUR} - 1$.

where, $\lambda = 1.867 \times 10^{-11}$/year^{-1} (Soderlund et al., 2004); $(^{176}Lu/^{177}Hf)_S$ and $(^{176}Hf/^{177}Hf)_S$ are the measured values of the samples; $(^{176}Lu/^{177}Hf)_{CHUR} = 0.0332$ and $(^{176}Hf/^{177}Hf)_{CHUR,0} = 0.282772$ (Blichert-Toft and Albarède, 1997); $(^{176}Lu/^{177}Hf)_{DM} = 0.0384$ and $(^{176}Hf/^{177}Hf)_{DM} = 0.28325$ (Griffin et al., 2002); $(^{176}Lu/^{177}Hf)_{mean\ crust} = 0.015$; $f_{cc} = [(^{176}Lu/^{177}Hf)_{mean\ crust}/(^{176}Lu/^{177}Hf)_{CHUR}] - 1$; $f_s = f_{Lu/Hf}$; $f_{DM} = [(^{176}Lu/^{177}Hf)_{DM}/(^{176}Lu/^{177}Hf)_{CHUR}] - 1$; t = crystallization time of zircon.
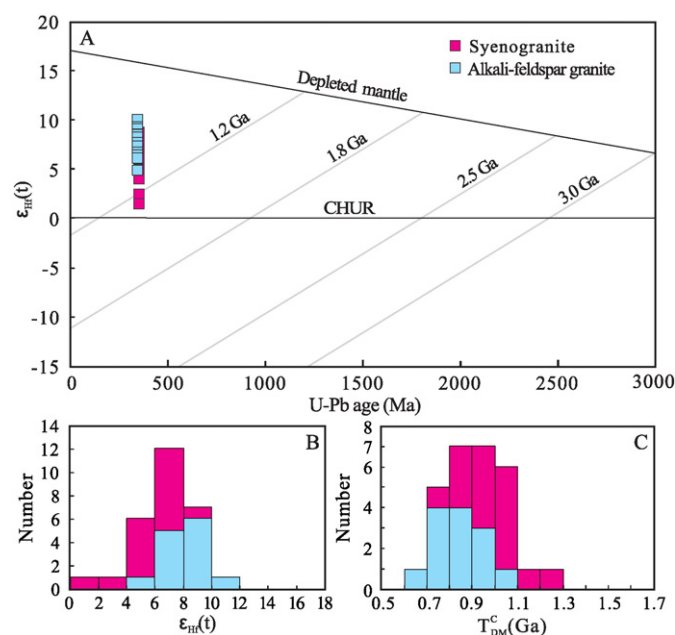
Fig. 10. (A) $\varepsilon_{Hf}(t)$ vs. U–Pb age diagram. (B) Histograms of zircon $\varepsilon_{Hf}(t)$ values. (C) Histograms of zircon Hf crustal model age (T^C_{DM}).

with those of reduced carbon that underwent a carbon isotopic exchange with carbonates in metasedimentary rocks (−15‰; Schidowski et al., 1983) and suggest metamorphic carbonate lithotypes as the source. The auriferous quartz veins also produced four high $\delta^{13}C_{CO2}$ values ranging from −6.8‰ to −5.2‰, which overlaps the values of igneous rocks (−30‰ to −3‰), atmospheric CO_2 (−11‰ to −7‰), continental crust (−7‰) and fluids from the mantle (−7‰ to −2‰; Cartigny et al., 1998; Chen et al., 2008). The Hongshi $\delta^{13}C_{CO2}$ values are consistent with those of various other orogenic gold deposits (−23 to +2‰; Ridley and Diamond, 2000; Zhou et al., 2014); therefore, the carbon isotopic compositions suggest a carbonaceous sedimentary source as the primary source of the carbon in the ore fluids in the Hongshi deposit.

Significant variation in the $\delta^{34}S$ values is observed in a few deposits; for example, the $\delta^{34}S$ values of the Zhenyuan deposit in southwest China range from −19.0‰ to +15.4‰ with a mean of −1.1‰ (Deng et al., 2015a), and those of the Qiangma deposit in central China vary from −5.8‰ to +8.8 ‰ with a mean of +2.5 ‰ (Zhou et al., 2015). By combining the new sulfur isotopic analyses in this study with published data (Wang et al., 2007), the $\delta^{34}S$ values of the 10 sulfide samples from the Hongshi deposit span a large range, with peaks varying from +1‰ to +4‰ (Fig. 11B; Table 5), falling within the range of most orogenic gold deposits (Fig. 12). The mixing of the different sources or the oxidation effect of a reduced fluid may explain a large range of $\delta^{34}S$ values (Deng et al., 2015a; Hodkiewicz et al., 2009; Liu et al., 2007). In this case, we suggest that the large $\delta^{34}S$ range may be attributed to the mixed sources. A possible sedimentary source is suggested by the two relatively low $\delta^{34}S$ values (−11.5‰ and −8.8‰). Therefore, a mixed source containing both magmatic rocks and sedimentary strata may be the source of sulfur in the fluids at Hongshi.

The values of $^{206}Pb/^{204}Pb$, $^{207}Pb/^{204}Pb$ and $^{208}Pb/^{204}Pb$ for the Hongshi auriferous pyrites are 18.235, 15.594, and 38.188, respectively (Table 5) (L.J. Wang et al., 2006). These lead isotopic values are within the range of those of sulfides from the Kanggur orogenic gold deposit in Eastern Tianshan (Wang et al., 2015c), suggesting that the two deposits have the same metal sources. The $^{207}Pb/^{204}Pb$ vs. $^{206}Pb/^{204}Pb$, and $^{208}Pb/^{204}Pb$ vs. $^{206}Pb/^{204}Pb$ diagrams shown in Fig. 11C and D demonstrate that the pyrite Pb isotope values in the Hongshi deposit are close to those of orogenic Pb (Doe and Zartman, 1979). These data suggest a relationship to an orogenic lead reservoir; thus, we suggest that the Hongshi fluid ore minerals have a Pb source similar to the Kanggur orogenic gold deposit.

In conclusion, the Hongshi gold deposit has fluid components and H–O–C–S–Pb isotopic signatures similar to the orogenic gold deposits (Y.J. Chen et al., 2012; Goldfarb et al., 2001; Groves et al., 1998; Wang et al., 2015c; Zhang et al., 2014). This suggests that the ore-forming fluids and metals may have originated from host rocks with some discernable magmatic source, perhaps with later remobilization during regional metamorphism (Pirajno et al., 1997; Pirajno, 2013).

5.3. Implications for geodynamic setting and gold metallogeny

The granitoid intrusion samples analyzed in this study were found to be enriched in LREEs and LILEs (e.g., Rb, K, Ba, and Pb) and depleted in HFSEs (e.g., Nb, Ta, P, and Ti), especially P and Ti, indicating a magma that formed in an arc setting (Liégeois et al., 1998). All the granitoid samples in this study fall within the volcanic arc field in the Ta vs. Yb and Rb–Hf–Ta tectonic discrimination diagrams (Fig. 13) (Harris et al., 1986; Pearce et al., 1984), which is characteristic of island arc granites emplaced during the Carboniferous subduction of an oceanic slab.

As reported in previous studies, widespread Late Paleozoic–Early Mesozoic granitoids and volcanic rocks were emplaced in the Eastern

Table 5
Summary of oxygen, hydrogen, carbon, sulfur, and lead isotopic compositions of Hongshi gold deposit ores.

Oxygen and hydrogen isotopic compositions				Carbon isotopic composition			Sulfur isotopic composition		Lead isotopic composition			
Mineral	T_h (°C)	$\delta^{18}O_w$(‰)	δD_w (‰)	Mineral	$\delta^{13}C_{CO2}$(‰)	$\delta^{13}C_{CH4}$(‰)	Mineral	$\delta^{34}S_{V\text{-}CDT}$/‰	Mineral	$^{206}Pb/^{204}Pb$	$^{207}Pb/^{204}Pb$	$^{208}Pb/^{204}Pb$
Quartz[a, f]	225	4.4	−104	Quartz[d, g]	−11.6	−28.8	Pyrite[c, f]	3	Pyrite[d, f]	18.235	15.594	38.188
Quartz[a, f]	230	4.4	−90	Quartz[d, g]	−10.1	−28.2	Pyrite[c, f]	1.4				
Quartz[a, f]	200	3.1	−95	Quartz[d, f]	−5.2		Pyrite[a, f]	0.4				
Quartz[a, g]	150	−0.3	−80	Quartz[d, f]	−6.8		Pyrite[a, f]	1.9				
Quartz[a, f]	225	4.9	−81	Quartz[d, f]	−5.8	−24.0	Pyrite[a, f]	1.1				
Quartz[a, g]	150	−1.7	−86	Quartz[d, f]	−5.8	−23.8	Pyrite[a, f]	1.4				
Quartz[a, f]	230	4.0	−91				Pyrite[a, f]	−11.5				
Quartz[a, e]	240	6.1	−63				Pyrite[a, f]	−8.8				
Quartz[b, f]	331.1	3.6	−86				Pyrite[a, f]	3.8				
Quartz[b, f]	342.7	7.4	−76				Pyrite[d, f]	4.2				

[a] Data from Wang et al. (2007).
[b] Data from Zhang et al. (2012).
[c] Data from this study.
[d] Data from L.J. Wang et al. (2006).
[e] Samples from mineralization stage I.
[f] Samples from mineralization stage II.
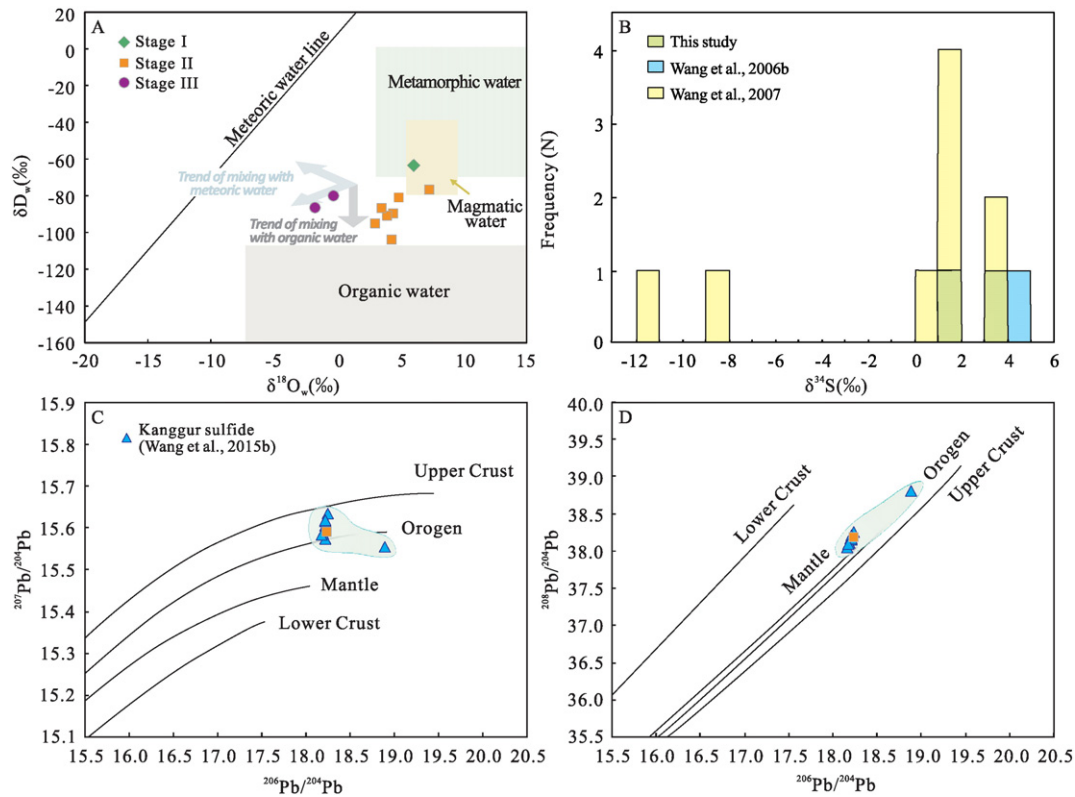[g] Samples from mineralization stage III.

Fig. 11. Mineral isotopic compositions of Hongshi gold deposit ores. (A) δD vs. δ^{18}O$_w$ diagram; the magmatic, metamorphic, and organic water fields are after Sheppard (1986), and the data are from Wang et al. (2007). (B) Sulfur isotopic compositions of pyrites; the data are from this study, L.J. Wang et al. (2006) and Wang et al. (2007). (C) ^{208}Pb/^{204}Pb vs. ^{206}Pb/^{204}Pb and (D) ^{207}Pb/^{204}Pb vs. ^{206}Pb/^{204}Pb plots showing the lead isotopic compositions; the data are from L.J. Wang et al. (2006) and Wang et al. (2015b).

Tianshan orogenic belt (Fig. 1C) (J.B. Wang et al., 2006) during a complex tectonic–magmatic evolution that included subduction and accretion followed by the collision between the Siberian and Tarim Cratons (Han et al., 2006; Rui et al., 2002; Santosh et al., 2011; Xiao et al., 2010, 2013). The above geodynamics can be summarized in two stages as follows: the double-sided subduction of the paleo-Tianshan oceanic plate during the Carboniferous formed the Dananhu–Tousuquan arc belt to the north and the Aqishan–Yamansu arc belt to the south, as evidenced by the positive bulk ε$_{Nd}$(t) and zircon ε$_{Hf}$(t) values of Carboniferous granitoids and volcanic rocks in Eastern Tianshan (Su et al., 2012; Wang et al., 2015a, 2015b; Zhang et al., 2015; and references there in); the post-collisional stage since the Early Permian, as supported by the presence of the youngest ophiolite of ~310 Ma along with widespread bimodal volcanic rocks of ~290 Ma (Qin et al., 2002; Su et al., 2012). Numerous Cu (+/−Ni), Au, Fe, and Ag metal deposits and associated magmatic rocks were formed in the periods of subduction and post-collisional tectonism.

The ages of the gold deposits within the Eastern Tianshan orogenic belt suggest a rapid metallogenic event during the Permian (Fig. 1C; Table 1). Rb–Sr and ^{39}Ar–^{40}Ar isochron methods constrained the ore-forming age of the Hongshi gold deposit to 262–254 Ma (W. Chen et al., 2007; Sun et al., 2012, 2013). Combined with the new SHRIMP zircon U–Pb ages presented herein (337–334 Ma), the recent isotopic ages mentioned above indicate that gold mineralization in the Hongshi area occurred later than granitoid emplacement in this area. Similar ages have been reported for other gold deposits in Eastern Tianshan. Zhang et al. (2002) reported four ages (290 ± 5, 282.3 ± 5, 258 ± 21, and 254 ± 7 Ma) for the Kanggur gold deposit based on the Rb–Sr dating of altered andesite and fluid inclusions extracted from auriferous quartz, while two plateau ages (246.9 ± 1.4 and 246.5 ± 1.1 Ma) were reported based on the ^{39}Ar–^{40}Ar dating of gold-related sericite from the Hongshan gold deposit (Chen et al., 2006). Moreover, Zhang et al. (2003b) obtained three Rb–Sr isochron ages (288 ± 7, 246 ± 7, and
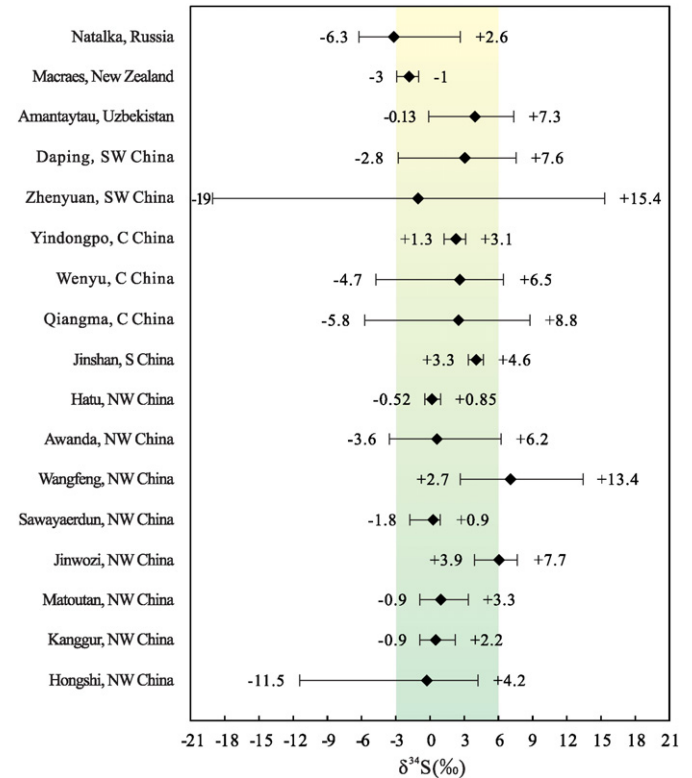

Fig. 12. Sulfur isotopic compositions of sulfide minerals from orogenic gold deposits. Data are from Wang et al. (2007, 2015b), Zhang et al. (2003a, 2013, 2014), Wu (2007), H.Y. Chen et al. (2012), Chen et al. (2000), Ding et al. (2014), Shen et al. (2015), Zhao et al. (2013), Zhou et al. (2014, 2015), Shi et al. (2010), Pasava et al. (2013), Craw et al. (1995), and Eremin et al. (1994).
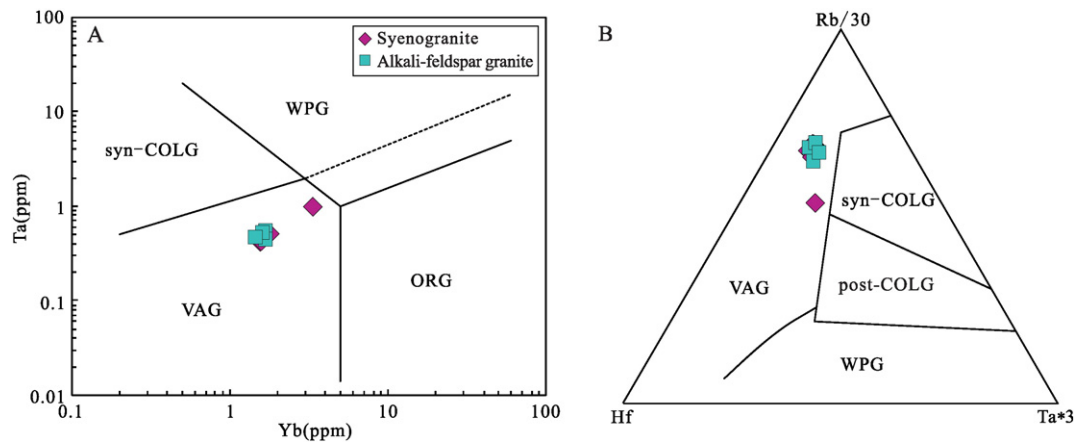
Fig. 13. Tectonic discrimination diagrams for the Hongshi granitoid intrusions: (A) Ta vs. Yb diagram (Pearce et al., 1984) and (B) Rb/30–Hf–Ta*3 diagram (Harris et al., 1986). WPG, within-plate granites; VAG, volcanic arc granites; Syn-COLG, syn-collision granites; Post-COLG, post-collision granites; ORG, ocean ridge granites.

244 ± 9 Ma) for the Shiyingtan gold deposit, and an ^{39}Ar–^{40}Ar plateau age of 243.2 ± 1.8 Ma was recently reported for the Jinwozi gold deposit by Wang et al. (2008). Although the above gold deposits exhibit isotopic data consistent with the gold mineralization age of the Hongshi deposit, they are located in or around the Kanggur–Huangshan ductile shear zone in Eastern Tianshan, for which Ma et al. (1993) reported an arenaceous mylonite Rb–Sr isochron age of 291.8 ± 28.5 Ma. Similarly, an Rb–Sr isochron age of 290 ± 5 Ma was reported by Zhang et al. (2002) for altered andesite, and W. Chen et al. (2005, 2007) determined ^{39}Ar–^{40}Ar ages of 262.9 ± 1.4 and 242.8 ± 1.5 Ma for mylonitic pyroclastic rock and mylonites from the ductile shear zone, respectively. Collectively, the shear deformation and metamorphism age of the Kanggur–Huangshan ductile shear zone is 291–242 Ma, which corresponds with the timing of gold mineralization in Eastern Tianshan. Thus, considering the coeval geological events and tectonic evolution in Eastern Tianshan, we suggest that the Hongshi gold mineralization occurred during a regime of ductile shear deformation and was possibly related to the post-collisional, Permian orogenesis event that affected much of Eastern Tianshan.

6. Conclusions

(1) The SHRIMP zircon U–Pb dating of syenogranite and alkalifeldspar granite indicates that the Hongshi gold deposit is younger than 334 Ma. The Hongshi granitoids have inhomogeneous $\varepsilon_{Hf}(t)$ values ranging from +1.5 to +10.1. The granitoids belong to the shoshonitic series, relatively enriched in Rb, K, Ba, and Pb and depleted in Nb, Ta, P, and Ti. The geochemical and isotopic characteristics suggest that the Hongshi granitoids derived from the melting of juvenile lower crust mixed with mantle components.

(2) The available fluid components and H–O–C–S–Pb isotopic signatures of the Hongshi deposit suggest that the predominant sources of the ore-forming fluids and metals are host rocks with some discernable magmatic sources, and that the Hongshi gold deposit is an orogenic-type system developed in the Eastern Tianshan orogenic belt during the Permian post-collisional tectonism.

(3) On the basis of the geochronology, petro-geochemistry and isotope data of the Hongshi gold deposit together with the deposit geology and regional geological evolution, we suggest that the Hongshi granitoids most likely acted as impermeable barriers that prevented the leakage and runoff of ore-bearing fluids, and played a key role in controlling gold mineralization.

References

Barbarin, B., 1999. A review of the relationships between granitoid types, their origins and their geodynamic environments. Lithos 46, 605–626.

Blichert-Toft, J., Albarède, F., 1997. The Lu–Hf geochemistry of chondrites and the evolution of the mantle–crust system. Earth Planet. Sci. Lett. 148, 243–258.

Boynton, W.V., 1984. Geochemistry of the Rare Earth Elements, Meteorite Studies. In: Henderson, P. (Ed.), Rare Earth Element Geochemistry. Elsevier, Amsterdam, p. 63-14.

Cao, J., Qiu, B., Chao, H.X., Ma, L.C., Yang, X.K., Sun, J.D., 2010. Characteristics of primary halos and prognosis of concealed ore bodies in the Hongshi gold deposit, Xinjiang. Acta Geosci. Sin. 31, 83–89 (in Chinese with English abstract).

Cartigny, P., Harris, J.W., Javoy, M., 1998. Eclogitic diamond formation at Jwaneng: no room for a recycled component. Science 280, 1421–1424.

Charvet, J., Shu, L.S., Charvet, S.L., 2007. Paleozoic structural and geodynamic evolution of eastern Tianshan (NW China): welding of the Tarim and Junggar plates. Episodes 30, 162–186.

Chen, H.Y., Bao, J.X., Zhang, Z.J., Liu, Y.L., Ni, P., Ling, H.F., 2000. Isotopic indication to source of ore materials and fluids of the Wangfeng gold deposit in Tianshan: a case study of metallogenesis during collisional orogenesis. Sci. China Ser. D Earth Sci. 43, 156–166.

Chen, F.W., Li, H.Q., Cai, H., Liu, H.Q., 1999. The origin of the Jinwozi gold deposit in Eastern Xinjiang: evidence from isotope geochronology. Geol. Rev. 45, 247–254 (in Chinese with English abstract).

Chen, Y.J., Pirajno, F., Qi, J.P., 2005a. Origin of gold metallogeny and sources of ore-forming fluids, Jiaodong Province, Eastern China. Int. Geol. Rev. 47, 530–549.

Chen, W., Sun, S., Zhang, Y., Xiao, W.J., Wang, Y.T., Wang, Q.L., Jiang, L.F., Yang, J.T., 2005b. ^{40}Ar/^{39}Ar geochronology of the Qiugemingtashi–Huangshan ductile shear zone in East Tianshan, Xinjiang, NW China. Acta Geol. Sin. 79, 790–804 (in Chinese with English abstract).

Chen, W., Zhang, Y., Zhao, H.B., Han, D., Wang, C.Y., 2006. East Tianshan mountain of Xinjiang Hongshan gold metallogenic era research. Geol. China 33, 632–640 (in Chinese with English abstract).

Chen, Y.J., Chen, H.Y., Zaw, K., Pirajno, F., Zhang, Z.J., 2007a. Geodynamic settings and tectonic model of skarn gold deposits in China: An overview. Ore Geol. Rev. 31, 139–169.

Chen, W., Zhang, Y., Qin, K.Z., Wang, Q.l., Wang, Y.T., Liu, X.Y., 2007b. Study on the age of the shear zone-type gold deposit of East Tianshan, Xinjiang, China. Acta Petrol. Sin. 23, 2007–2016 (in Chinese with English abstract).

Chen, Y.J., Pirajno, F., Qi, J.P., 2008. The Shanggong gold deposit, Eastern Qinling Orogen, China: isotope geochemistry and implications for ore genesis. J. Asian Earth Sci. 33, 252–266.

Chen, Y.J., Pirajno, F., Wu, G., Qi, J.P., Xiong, X.L., 2012a. Epithermal deposits in North Xinjiang, NW China. Int. J. Earth Sci. 101, 889–917.

Chen, H.Y., Chen, Y.J., Baker, M., 2012b. Isotopic geochemistry of the Sawayaerdun orogenic-type gold deposit, Tianshan, northwest China: implications for ore genesis and mineral exploration. Chem. Geol. 310, 1–11.

Chen, J., Santosh, M., Somerville, I., Chen, H.Y., 2014. Indosinian tectonics and mineral systems in China: an introduction. Geol. J. 49, 331–337.

Craw, D., Hall, A.J., Fallick, A.E., Boyce, A.J., 1995. Sulfur isotopes in a metamorphogenic gold deposit, Macraes Mine, Otago Schist, New Zealand. N. Z. J. Geol. Geophys. 38, 131–136.

Deng, J., Wang, Q.F., 2015. Gold mineralization in China: metallogenic provinces, deposit types and tectonic framework. Gondwana Res. http://dx.doi.org/10.1016/j.gr.2015.10.003.

Deng, J., Wang, Q.F., Li, G.J., Santosh, M., 2014. Cenozoic tectono-magmatic and metallogenic processes in the Sanjiang region, southwestern China. Earth-Sci. Rev. 138, 268–299.

Deng, J., Wang, Q.F., Li, G.J., Zhao, Y., 2015a. Structural control and genesis of the Oligocene Zhenyuan orogenic gold deposit, SW China. Ore Geol. Rev. 65, 42–54.

Deng, J., Wang, C.M., Bagas, L., Carranza, E.J.M., Lu, Y.J., 2015b. Cretaceous–Cenozoic tectonic history of the Jiaojia Fault and gold mineralization in the Jiaodong Peninsula, China: constraints from zircon U–Pb, illite K–Ar, and apatite fission track thermochronometry. Mineral. Deposita http://dx.doi.org/10.1007/S00126-015-0584-1.

Ding, Q.F., Wu, C.Z., Santosh, M., Fu, Y., Dong, L.H., Qu, X., Gu, L.X., 2014. H–O, S and Pb isotope geochemistry of the Awanda gold deposit in southern Tianshan, Central Asian orogenic belt: implications for fluid regime and metallogeny. Ore Geol. Rev. 62, 40–53.

Doe, B.R., Zartman, R.E., 1979. Plumbotectonics of the Phanerozoic. In: Barnes, H.L. (Ed.), Geochemistry of Hydrothermal Ore Deposits. John Wiley, New York, pp. 22–70.

Eremin, R.A., Voroshin, S.V., Sidorov, V.A., Shakhtyrov, V.G., Pristavko, V.A., Gashtold, V.V., 1994. Geology and genesis of the Natalka gold deposit, Northeast Russia. Int. Geol. Rev. 36, 1113–1138.

Giggenbach, W.F., 1995. Variations in the chemical and isotopic composition of fluids discharged from the Taupo Volcanic Zone, New Zealand. J. Volcanol. Geotherm. Res. 68, 89–116.

Goldfarb, R.J., Groves, D.I., Gardoll, S., 2001. Orogenic gold and geologic time: a global synthesis. Ore Geol. Rev. 18, 1–75.

Goldfarb, R.J., Taylor, R.D., Collins, G.S., Goryachev, N.A., Orlandini, O.F., 2014. Phanerozoic continental growth and gold metallogeny of Asia. Gondwana Res. 25, 48–102.

Green, T.H., 1995. Significance of Nb/Ta as an indicator of geochemical processes in the crust–mantle system. Chem. Geol. 120, 347–359.

Griffin, W., Wang, X., Jackson, S., Pearson, N., O'Reilly, S.Y., Xu, X., Zhou, X., 2002. Zircon chemistry and magma mixing, SE China: in-situ analysis of Hf isotopes, Tonglu and Pingtan igneous complexes. Lithos 61, 237–269.

Groves, D.I., Goldfarb, R.J., Gebre-Mariam, M., Hagemann, S.G., Robert, F., 1998. Orogenic gold deposit: a proposed classification in the context of their crustal distribution and relationship to other gold deposit types. Ore Geol. Rev. 13, 7–27.

Han, C.M., Xiao, W.J., Zhao, G.C., Mao, J.W., Li, S.Z., Yan, Z., Mao, Q.G., 2006. Major types, characteristics and geodynamic mechanism of Upper Paleozoic copper deposits in northern Xinjiang, north western China. Ore Geol. Rev. 28, 308–328.

Harris, H.B.W., Pearce, J.A., Tiandle, A.G., 1986. Geochemical characteristics of collision-zone magmatism. Spec. Publ. Geol. Soc. Lond. 19, 67–81.

Hodkiewicz, P.F., Groves, D.I., Davidson, G.J., Weinberg, R.F., Hagemann, S.G., 2009. Influence of structural setting on sulfur isotopes in Archean orogenic gold deposits, Eastern Goldfields Province, Yilgarn, Western Australia. Mineral. Deposita 44, 129–150.

Hou, K.J., Li, Y.H., Zou, T.R., Qu, X.M., Shi, Y.R., Xie, G.Q., 2007. Laser ablation-MC-ICP-MS technique for Hf isotope microanalysis of zircon and its geological applications. Acta Petrol. Sin. 23, 2595–2604 (in Chinese with English abstract).

Huang, X.W., Qi, L., Gao, J.F., Zhou, M.F., 2013. First reliable Re–Os Ages of pyrite and stable isotope compositions of Fe(-Cu) deposits in the Hami Region, Eastern Tianshan Orogenic Belt, NW China. Resour. Geol. 63, 166–187.

Kovalenko, V.I., Yarmolyuk, V.V., Kovach, V.P., Kotov, A.B., Kozakov, I.K., Salnikova, E.B., Larin, A.M., 2004. Isotopic provinces, mechanism of generation and sources of the continental crust in the Central Asian mobile belt: geological and isotopic evidence. J. Asian Earth Sci. 23, 605–627.

Le Maitre, R.W., 1989. A Classification of Igneous Rocks and Glossary of Terms. Blackwell, Oxford, p. 103.

Li, H.Q., Xie, C.F., Chang, H.L., 1998. Study on Metallogenetic Chronology of Nonferrous and Precious Metallic ore Deposits in Northern Xinjiang, China. Geological Publishing House, Beijing, pp. 1–267 (in Chinese).

Li, S., Wang, T., Wilde, S.A., Tong, Y., 2013. Evolution, source and tectonic significance of Early Mesozoic granitoid magmatism in the Central Asian Orogenic Belt (central segment). Earth Sci. Rev. 126, 206–234.

Li, Q., Santosh, M., Li, S.R., Zhang, J.Q., 2015. Petrology, geochemistry and zircon U–Pb and Lu–Hf isotopes of the Cretaceous dykes in the central North China Craton: implications for magma genesis and gold metallogeny. Ore Geol. Rev. 67, 57–77.

Liégeois, J.P., Navez, J., Hertogen, J., Black, R., 1998. Contrasting origin of post-collisional high–K calc-alkaline and shoshonitic versus alkaline and peralkaline granitoids. The use of sliding normalization. Lithos 45, 1–28.

Liu, D.Y., Jian, P., Kröner, A., Xu, S.T., 2006. Dating of prograde metamorphic events deciphered from episodic zircon growth in rocks of the Dabie-Sulu UHP complex, China. Earth Planet. Sci. Lett. 250, 650–666.

Liu, J.J., Zheng, M.H., Cook, N.J., Long, X.R., Deng, J., Zhai, Y.S., 2007. Geological and geochemical characteristics of the Sawaya'erdun gold deposit, southwestern Chinese Tianshan. Ore Geol. Rev. 32, 125–156.

Ludwig, K.R., 2003. User's manual for Isoplot 3.0, a geochronological tool kit for Microsoft Excel: Berkeley, CA. Geochronol. Cent. Spec. Publ. 4, 25–32.

Ma, R.S., Wang, Y.Y., Ye, S.F., 1993. Tectonic Framework and Crustal Evolution, East Tianshan. Publishing House of Nanjing University, Nanjing, pp. 1–265 (in Chinese with English abstract).

Maniar, P.D., Piccoli, P.M., 1989. Tectonic discrimination of granitoids. Geol. Soc. Am. Bull. 101, 635–643.

Mao, J.W., Goldfarb, R.T., Wang, Y.T., Hart, C.J., Wang, Z.L., Yang, J.M., 2005. Late Paleozoic base and precious metal deposits, East Tianshan, Xinjiang, China: characteristics and geodynamic setting. Episodes 28, 1–14.

Mao, J.W., Pirajno, F., Lehmannn, B., Luo, M.C., Berzina, N., 2014. Distribution of porphyry deposits in the Eurasian continent and their corresponding tectonic settings. J. Asian Earth Sci. 79, 576–584.

Mo, X.X., Dong, G.C., Zhao, Z.D., Zhu, D.C., Zhou, S., Niu, Y., 2009. Mantle input to the crust in southern Gangdese, Tibet, during the Cenozoic: zircon Hf isotopic evidence. J. Earth Sci. 20, 241–249.

Norrish, K., Hutton, J.T., 1969. An accurate X-ray spectrographic method for analysis of a wide range of geological samples. Geochim. Cosmochim. Acta 48, 1523–1536.

Pasava, J., Frimmel, H., Vymazalová, A., Dobes, P., Jukov, A., Koneev, R., 2013. A two-stage evolution model for the Amantaytau orogenic-type gold deposit in Uzbekistan. Mineral. Deposita 48, 825–840.

Pearce, J.A., Harris, N.B.W., Tindle, A.C., 1984. Trace element discrimination diagrams for the tectonic interpretation of granitic rocks. J. Petrol. 25, 956–983.

Pirajno, F., 2010. Intracontinental strike–slip faults, associated magmatism, mineral systems and mantle dynamics: examples from NW China and Altay–Sayan (Siberia). J. Geodyn. 50, 325–346.

Pirajno, F., 2013. The Geology and Tectonic Settings of China's Mineral Deposits. Springer, Berlin, pp. 1–671.

Pirajno, F., Luo, Z.Q., Liu, S.F., Dong, L.H., 1997. Gold deposits in the Eastern Tian Shan, Northwestern China. Int. Geol. Rev. 39, 891–904.

Pirajno, F., Seltmann, R., Yang, Y.Q., 2011. A review of mineral systems and associated tectonic settings of northern Xinjiang, NW China. Geosci. Front. 2, 157–185.

Qi, L., Hu, J., Gregoire, D.C., 2000. Determination of trace elements in granites by inductively coupled plasma mass spectrometry. Talanta 51, 507–513.

Qin, K.Z., Fang, T.H., Wang, S.L., Zhu, B.Q., Feng, Y.M., Yu, H.F., Xiu, Q.Y., 2002. Plate tectonic division, evolution and metallogenic settings in eastern Tianshan mountains. NW China Xinjiang Geol. 20, 302–308 (in Chinese with English abstract).

Qin, K.Z., Su, B.X., Sakyi, P.A., Tang, D.M., Li, X.H., Sun, H., Xiao, Q.H., Liu, P.P., 2011. S1MS zircon U–Pb geochronology and Sr–Nd isotopes of Ni–Cu bearing mafic–ultramafic intrusions in eastern Tianshan and Beishan in correlation with flood basalts in Tarim Basin (NW China): constraints on a ca. 280 Ma mantle plume. Am. J. Sci. 311, 237–260.

Rapp, R.P., Watson, E.B., 1995. Dehydration melting of metabasalt at 8–32 kbar: implications for continental growth and crust–mantle recycling. J. Petrol. 36, 891–931.

Ridley, J.R., Diamond, L.W., 2000. Fluid Chemistry of Orogenic Lode Gold Deposits and Implications for Genetic Models. In: Hagemann, S.G., Brown, P.E. (Eds.), Gold in 2000. Reviews in Economic Geology 13, pp. 141–162.

Rui, Z.Y., Richard, J., Goldfarb, Qiu, Y.M., Pirajno, F., Yun, G., 2002. Paleozoic-early Mesozoic gold deposits of the Xinjiang Autonomous Region, northwestern China. Mineral. Deposita 37, 393–418.

Santosh, M., Kusky, T., Wang, L., 2011. Supercontinent cycles, extreme metamorphic processes, and changing fluid regimes. Int. Geol. Rev. 53, 1403–1423.

Schidowski, M., Hayes, J.M., Kaplan, I.R., 1983. Isotopic Inferences of Ancient Biochemistry: Carbon, Sulfur, Hydrogen and Nitrogen. In: Schopf, J.W. (Ed.), Earth's Earliest Biosphere. Princeton University Press, Princeton, NJ, pp. 149–186.

Sengor, A.M.C., Natal'in, B.A., Burtman, V.S., 1993. Evolution of the Altaid tectonic collage and Palaeozoic crustal growth in Eurasia. Nature 364, 299–307.

Shen, P., Xiao, W., Pan, H., Dong, L., Li, C., 2013. Petrogenesis and tectonic settings of the Late Carboniferous Jiamantieliek and Baogutu ore-bearing porphyry intrusions in the southern West Junggar, NW China. J. Asian Earth Sci. 75, 158–173.

Shen, P., Pan, H., Zhu, H., 2015. Two fluid sources and genetic implications for the Hatu gold deposit, Xinjiang, China. Ore Geol. Rev. http://dx.doi.org/10.1016/j.oregeorev.2015.03.008.

Sheppard, S., 1986. Characterization and isotopic variations in natural waters. Rev. Mineral. Geochem. 16, 165–183.

Shi, G.Y., Sun, X.M., Zhang, Y., Xiong, D.X., Zhai, W., Pan, W.J., Hu, B.M., 2010. H-O-C-S isotopic of ore forming fluids in Daping gold deposit in Ailaoshan gold belt, Yunan province, China. Acta Petrol. Sin. 26, 1751–1759 (in Chinese with English abstract).

Soderlund, U., Patchett, P.J., Vervoort, J.D., Isachsen, C.E., 2004. The ^{176}Lu decay constant determined by Lu–Hf and U–Pb isotope systematics of Precambrian mafic intrusions. Earth Planet. Sci. Lett. 219, 311–324.

Su, B.X., Qin, K.Z., Sun, H., Tang, D.M., Xiao, Q.H., Liu, P.P., 2012. Olivine compositional mapping of mafic–ultramafic complexes in Eastern Xinjiang (NW China): implications for Cu–Ni mineralization and tectonic dynamics. J. Earth Sci. 23, 41–53.

Sun, S.S., McDonough, W.F., 1989. Chemical and Isotopic Systematics of Oceanic Basalts, Implications for Mantle Composition and Processes. In: Saunders, A.D., Norry, M.J.

(Eds.), Magmatism in Ocean Basins. London Geological Society Special Publication 42, pp. 313–345.

Sun, J.B., Chen, W., Liu, X.Y., Zhang, Y., Li, J., Ji, H.W., Zhang, B., 2012. Ar–Ar and zircon U–Pb dating of quartz albitophyres in the Hongshi gold ore district of Eastern Tianshan and its metallogenic significance. Acta Geosci. Sin. 33, 907–917 (in Chinese with English abstract).

Sun, J.B., Zhang, L.M., Chen, W., Li, H.Q., Zhang, Y., Liu, X.Y., Li, J., 2013. Quartz Rb–Sr isotopic dating of Hongshi gold deposit in East Tianshan Mountains. Geol. Rev. 59, 382–388 (in Chinese with English abstract).

Sylvester, P.J., 1998. Post-collisional strongly peraluminous granites. Lithos 45, 29–44.

Tatsumi, Y., Eggins, S., 1995. Subduction Zone Magmatism. Blackwell Publishing, Boston.

Wang, J.B., Wang, Y.W., He, Z.J., 2006a. Ore deposits as a guide to the tectonic evolution in the East Tianshan Mountains, NW China. Geol. China 33, 461–469 (in Chinese with English abstract).

Wang, L.J., Wang, J.B., Wang, Y.W., Zhu, H.P., 2006b. S, Pb, C isotopes geochemistry from gold deposits in Junggar–East Tianshan mountains area and the indication for gold mineralization, North Xinjiang. Acta Geol. Sin. 22, 1437–1447 (in Chinese with English abstract).

Wang, Y.T., Zhang, W.Z., Wang, L., Mao, J.W., Yang, F.Q., Chen, W., 2007. Tracing the sources of ore-forming fluids and materials of the Hongshi gold deposit in the Eastern Tianshan, Xinjiang, NW China. Acta Petrol. Sin. 23, 1998–2006 (in Chinese with English abstract).

Wang, Q.L., Chen, W., Han, D., Wang, C.Y., Liu, X.Y., Zhang, S.H., 2008. Xinjiang Jinwozi gold deposit formation is discussed research and genetic mechanism. Geol. China 35, 286–291 (in Chinese with English abstract).

Wang, Y.H., Xue, C.J., Liu, J.J., Wang, J.P., Yang, J.T., Zhang, F.F., Zhao, Z.N., Zhao, Y.J., 2014. Geochemistry, geochronology, Hf isotope, and geological significance of the Tuwu porphyry copper deposit in Eastern Tianshan, Xinjiang. Acta Petrol. Sin. 30, 3383–3399 (in Chinese with English abstract).

Wang, Y.H., Xue, C.J., Liu, J.J., Wang, J.P., Yang, J.T., Zhang, F.F., Zhao, Z.N., Zhao, Y.J., Liu, B., 2015a. Early carboniferous adakitic rocks in the area of the Tuwu deposit, eastern Tianshan, NW China: slab melting and implications for porphyry copper mineralization. J. Asian Earth Sci. 103, 332–349.

Wang, Y.H., Xue, C.J., Wang, J.P., Peng, R.M., Yang, J.T., Zhang, F.F., Zhao, Z.N., Zhao, Y.J., 2015b. Petrogenesis of magmatism in the Yandong region of Eastern Tianshan, Xinjiang: geochemical, geochronological and Hf isotope constraints. Int. Geol. Rev. 57, 1130–1151.

Wang, Y.H., Xue, C.J., Zhang, F.F., Liu, J.J., Gao, J.B., Qi, T.J., 2015c. SHRIMP zircon U–Pb geochronology, geochemistry and H–O–Si–S–Pb isotope systematics of the Kanggur gold deposit in Eastern Tianshan, NW China: implication for ore genesis. Ore Geol. Rev. 68, 1–13.

Wang, Y.H., Zhang, F.F., Liu, J.J., Xue, C.J., Wang, J.P., Liu, B., Lu, W.W., 2015d. Petrogenesis of granites in Baishan molybdenum deposit, eastern Tianshan, Xinjiang: zircon U–Pb geochronology, geochemistry, and Hf isotope constraints. Acta Petrol. Sin. 31, 1962–197 (in Chinese with English abstract).

Wang, Y.H., Zhao, C.B., Zhang, F.F., Liu, J.J., Wang, J.P., Peng, R.M., Liu, B., 2015e. SIMS zircon U–Pb and molybdenite Re–Os geochronology, Hf isotope, and whole-rock geochemistry of the Wunugetushan porphyry Cu–Mo deposit and granitoids in NE China and their geological significance. Gondwana Res. 28, 1228–1245.

Windley, B.F., Alexeiev, D., Xiao, W., Kröner, A., Badarch, G., 2007. Tectonic models for accretion of the Central Asian Orogenic Belt. J. Geol. Soc. Lond. 164, 31–47.

Wu, F.Y., Yang, Y.H., Xie, L.W., Yang, J.H., Xu, P., 2006. Hf isotopic compositions of the standard zircons and bad–deleyites used in U–Pb geochronology. Chem. Geol. 234, 105–126.

Wu, F.Y., Li, X.H., Yang, J.H., Zheng, Y.F., 2007. Discussions on the petrogenesis of granites. Acta Petrol. Sin. 23, 1217–1238 (in Chinese with English abstract).

Xiao, W.J., Huang, B.C., Han, C.M., Sun, S., Li, J.L., 2010. A review of the western part of the Altaids: a key to understanding the architecture of accretionary orogens. Gondwana Res. 18, 253–273.

Xiao, W.J., Windley, B.E., Allen, M.B., Han, C.M., 2013. Paleozoic multiple accretionary and collisional tectonics of the Chinese Tianshan orogenic collage. Gondwana Res. 23, 1316–1341.

Xinjiang Bureau of Geology and Mineral Resources, No.1 Geological Party, 2003. The geological survey report of the Hongshi gold deposit in Shanshan area, Xinjiang.

Xue, C.J., Ji, J.S., Zeng, Z.R., 1995. The different types of gold deposits and mineralization in Kanggur gold belt, East Tianshan. Northwest. Geol. 16, 30–36 (in Chinese with English abstract).

Yang, X.K., Tao, H.X., Luo, G.C., Ji, J.S., 1996. Basic features of plate tectonics in Eastern Tianshan of China. Xinjiang Geol. 14, 221–227 (in Chinese with English abstract).

Yang, F.Q., Mao, J.W., Bierlein, F.P., Pirajno, F., Zhao, C.S., Ye, H.S., Liu, F., 2009. A review of the geological characteristics and geodynamic mechanisms of Late Paleozoic epithermal gold deposits in North Xinjiang, China. Ore Geol. Rev. 35, 217–234.

Zhai, Y.S., Deng, J., Li, X.B., 1999. Essentials of Metallogeny. Geological Publishing House, Beijing, China, pp. 1–287 (in Chinese with English abstract).

Zhai, Y.S., Yao, S.Z., Cai, K.Q., 2011. Mineral Deposits. 3rd edition. Geological Publishing House, Beijing (in Chinese).

Zhang, L.C., Ji, J.S., Zeng, Z.R., 1999. Geochemical characteristics and source of mineralizing fluid of Kangurtag gold deposit, East Tianshan. Geochimica 28, 18–25 (in Chinese with English abstract).

Zhang, L.C., Liu, T.B., Shen, Y.C., Li, G.M., Ji, J.S., 2002. Isotopic geochronology of the Late Paleozoic Kanggur gold deposit of East Tianshan Mountains, Xinjiang, NW China. Resour. Geol. 53, 249–261.

Zhang, L.C., Shen, Y.C., Ji, J.S., 2003a. Characteristics and genesis of Kanggur gold deposit in the eastern Tianshan mountains, NW China: evidence from geology, isotope distribution and chronology. Ore Geol. Rev. 23, 71–90.

Zhang, L.C., Ji, J.S., Qin, K.Z., Yang, X.K., Xie, C.J., Feng, C.Y., 2003b. Geological and Geochemical Features of Shiyingtan Permian low Sulfidation Epithermal Gold Deposit, Eastern Tianshan, NW China. In: Mao, Goldfarb, Seltmann, Wang, Xiao, Hart (Eds.), Tectonic Evolution and Metallogeny of the Chinese Altay and Tianshan. Proceedings Volume of the International Symposium on IGCP–473 project. AGOD Guidebook Series 10, pp. 261–270.

Zhang, D.Y., Zhou, T.F., Yuan, F., Fan, Y., Liu, S., Ning, F.Q., Sum, H.H., 2012. Ore-forming fluids of main Au deposits in western Kangguer shear zone of Eastern Tianshan Mountains and their geological implications. Mineral Deposits 31, 555–568 (in Chinese with English abstract).

Zhang, J., Chen, Y.J., Franco, P., Deng, J., Chen, H.Y., Wang, C.M., 2013. Geology, C–H–O–S–Pb isotope systematics and geochronology of the Yindongpo gold deposit, Tongbai Mountains, central. Ore Geol. Rev. 53, 343–356.

Zhang, Z.J., Chen, H.Y., Hu, M.Y., Zhang, J., Li, D.F., 2014. Isotopic geochemistry of the Jinwozi gold deposit in the eastern Tianshan orogen, NW China: implications for the ore genesis. Geol. J. 49, 574–583.

Zhang, F.F., Wang, Y.H., Liu, J.J., Wang, J.P., 2015. Zircon U–Pb and molybdenite Re–Os geochronology, Hf isotope analyses, and whole-rock geochemistry of the Donggebi Mo deposit, eastern Tianshan, Northwest China, and their geological significance. Int. Geol. Rev. 57, 446–462.

Zhao, C., Ni, P., Wang, G.G., Ding, J.Y., Chen, H., Zhao, K.D., Xu, Y.F., 2013. Geology, fluid inclusion, and isotope constraints on ore genesis of the Neoproterozoic Jinshan orogenic gold deposit, South China. Geofluids 13, 506–527.

Zhou, T.F., Yuan, F., Zhang, D.Y., Fan, Y., Liu, S., Peng, M.X., Zhang, J.D., 2010. Geochronology, tectonic setting and mineralization of granitoids in ueluotage area, eastern Tianshan, Xinjiang. Acta Petrol. Sin. 26, 478–502 (in Chinese with English abstract).

Zhou, Z.J., Chen, Y.J., Jiang, S.Y., Zhao, H.X., Qin, Y., Hu, C.J., 2014. Geology, geochemistry and ore genesis of the Wenyu gold deposit, Xiaoqinling gold field, Qinling Orogen, southern margin of North China Craton. Ore Geol. Rev. 59, 1–20.

Zhou, Z.J., Chen, Y.J., Jiang, S.Y., Hu, C.J., Qin, Y., Zhao, H.X., 2015. Isotope and fluid inclusion geochemistry and genesis of the Qiangma gold deposit, Xiaoqinling gold field, Qinling Orogen, China. Ore Geol. Rev. 66, 47–64.

Zhu, D.C., Zhao, Z.D., Niu, Y.L., Dilek, Y., Hou, Z.Q., Mo, X.X., 2013. The origin and pre-Cenozoic evolution of the Tibetan Plateau. Gondwana Res. 23, 1429–1454.